

ROTATION-SUPPORTED NEUTRINO-DRIVEN SUPERNOVA EXPLOSIONS IN THREE DIMENSIONS AND THE CRITICAL LUMINOSITY CONDITION

ALEXANDER SUMMA¹, HANS-THOMAS JANKA¹, TOBIAS MELSON¹, AND ANDREAS MAREK²

¹Max-Planck-Institut für Astrophysik, Karl-Schwarzschild-Str. 1, D-85748 Garching, Germany,
email: thj@mpa-garching.mpg.de

²Max Planck Computing and Data Facility (MPCDF), Gießenbachstr. 2, D-85748 Garching, Germany

ABSTRACT

We present the first self-consistent, three-dimensional (3D) core-collapse supernova simulations performed with the PROMETHEUS-VERTEX code for a rotating progenitor star. Besides using the angular momentum of the $15 M_{\odot}$ model as obtained in the stellar evolution calculation with an angular frequency of $\sim 10^{-3} \text{ rad s}^{-1}$ (spin period of more than 6000 s) at the Si/Si-O interface, we also computed 2D and 3D cases with no rotation and with a ~ 300 times shorter rotation period and different angular resolutions. In 2D, only the nonrotating and slowly rotating models explode, while rapid rotation prevents an explosion within 500 ms after bounce because of lower radiated neutrino luminosities and mean energies and thus reduced neutrino heating. In contrast, only the fast rotating model develops an explosion in 3D when the Si/Si-O interface collapses through the shock. The explosion becomes possible by the support of a powerful SASI spiral mode, which compensates for the reduced neutrino heating and pushes strong shock expansion in the equatorial plane. Fast rotation in 3D leads to a “two-dimensionalization” of the turbulent energy spectrum (yielding roughly a -3 instead of a $-5/3$ power-law slope at intermediate wavelengths) with enhanced kinetic energy on the largest spatial scales. We also introduce a generalization of the “universal critical luminosity condition” of Summa et al. (2016) to account for the effects of rotation, and demonstrate its viability for a set of more than 40 core-collapse simulations including 9 and $20 M_{\odot}$ progenitors as well as black-hole forming cases of 40 and $75 M_{\odot}$ stars to be discussed in forthcoming papers.

Keywords: supernovae: general — hydrodynamics — instabilities — neutrinos

1. INTRODUCTION

Although recent three-dimensional (3D) simulations of core-collapse supernovae (CCSN) were able to yield successful explosions for a variety of progenitor stars and showed the viability of the neutrino-driven explosion mechanism in principle (see, e.g., Takiwaki et al. 2012, 2014; Lentz et al. 2015; Melson et al. 2015b,a; Müller 2016; Roberts et al. 2016), 3D models seem to be less prone to explosion than their corresponding axisymmetric (2D) counterparts (for an extensive review see Janka et al. 2016). Due to the extreme computational demands of 3D simulations including energy-dependent neutrino transport treatments, the numerical resolution in current 3D models is still limited. While the influence of this deficit on the explosion physics remains to be investigated in fully self-consistent supernova simulations, the enhanced reluctance to explosion in 3D may also point towards important physical ingredients that have not yet been considered in the latest 3D simulations.

In order to get robust and sufficiently energetic neutrino-powered explosions, several solutions providing

additional support to the neutrino-driven mechanism have been proposed up to now. Even though many of these ideas have already been investigated in the context of 1D and 2D simulations, final conclusions heavily rely on simulations without imposed symmetry constraints because of the three-dimensional nature of the expected effects. The era of sophisticated 3D simulations has just begun and first steps towards the inclusion of additional physics have been made recently. These comprise the consideration of progenitor properties such as pre-collapse perturbations (Couch & Ott 2013; Couch et al. 2015; Müller & Janka 2015; Müller et al. 2016; Müller 2016; Müller et al. 2017), rotation (Kuroda et al. 2014; Nakamura et al. 2014; Takiwaki et al. 2016), and magnetic fields (Winteler et al. 2012; Mösta et al. 2014), as well as the exploration of changes in the microphysics, which could enhance the neutrino heating behind the shock (Melson et al. 2015a; Bollig et al. 2017).

In the present work we focus on the possible support of neutrino-driven supernova explosions by rotation. The effects of rotation are of great interest in the context

of CCSNe, because the angular momentum of the stellar core can influence both the explosion physics and the birth properties of the neutron star (e.g. Ott et al. 2006). While rapid rotation is a key prerequisite for explosion scenarios such as the magnetorotational mechanism (Akiyama et al. 2003; Dessart et al. 2007; Winteler et al. 2012; Mösta et al. 2014, 2015; Obergaulinger & Aloy 2017) or models developing the low- T/W spiral instability (Takiwaki et al. 2016), large rotation rates are generally not expected for progenitors of typical type IIP CCSNe (Heger et al. 2005). Asteroseismic measurements of evolved low-mass stars point towards an efficient spin-down mechanism of the core (Cantiello et al. 2014). Models including the angular momentum transport by magnetic fields predict pre-collapse angular momenta with peak values of the order of $10^{15} \text{ cm}^2 \text{ s}^{-1}$ at a mass coordinate of $1.5 M_{\odot}$ (Heger et al. 2005). Furthermore, no efficient mechanism is known which could slow down a new-born (sub-)millisecond-period neutron star resulting from a rapidly rotating iron core to the typical observed periods of tens to hundreds of milliseconds of young pulsars (Ott et al. 2006). Simplified simulations point towards a subtle interplay between rotation and the growth of the spiral mode of the standing accretion-shock instability (SASI) even for moderate rotation rates (Blondin & Mezzacappa 2007; Iwakami et al. 2009; Blondin et al. 2017; Kazeroni et al. 2017), calling for thorough investigations with sophisticated explosion models taking into account full neutrino physics.

For the first time, we present the results of rotating, self-consistent 3D simulations with the PROMETHEUS-VERTEX code applying the most complete set of neutrino interactions currently available. In our study, we consider a $15 M_{\odot}$ progenitor from the stellar evolution calculations of Heger et al. (2005), which include rotation and angular momentum transport by magnetic fields. In addition to the rotation profile inferred from Heger et al. (2005), we perform simulations for the same progenitor, but with enhanced angular velocities as previously applied in Buras et al. (2006a) and Marek & Janka (2009). In total, our study consists of five 3D and six 2D models with different resolutions and rotation rates. Since many 2D studies concerning the influence of rotation on the explosion physics and the final neutron star spin have already been conducted up to now (see, e.g., Kotake et al. 2006; Ott et al. 2006), we only provide a brief comparison of the axisymmetric models to their 3D counterparts and center our discussion of the results on the two best resolved 3D simulations.

In multidimensional simulations, the beginning of runaway shock expansion seems to be characterized by a huge model-to-model variance in the diagnostic parameters such as neutrino luminosity, neutrino heating rate and efficiency, shock radius, mass-accretion rate, tur-

bulent kinetic and total energy in the gain layer, and so on. This naturally raises the question if any combination of the relevant parameters reliably signals the onset of shock expansion. Extending the critical luminosity condition introduced by Burrows & Goshy (1993) from spherical symmetry to the multidimensional case, Summa et al. (2016) showed that the consideration of turbulent mass motions in the gain layer through an isotropic pressure contribution (cf. Müller & Janka 2015) leads to a generalized criterion which captures the conditions needed for shock runaway in a large set of 2D models remarkably well.

A reduction of the critical luminosity of shock runaway due to rotation and SASI spiral modes has been demonstrated with 3D simulations by Iwakami et al. (2014) and Nakamura et al. (2014). However, both studies use a simple light-bulb treatment for the neutrino emission, which is unable to capture the feedback effects of rotation on the neutrino transport. In contrast, our models are fully self-consistent in the sense that they evolve the neutrino transport coupled with the hydrodynamics of the stellar plasma. Moreover, a subset of our 2D and 3D simulations are started from the angular momentum profile provided by a stellar evolution calculation up to the onset of iron-core collapse performed by Heger et al. (2005).

The coupling of neutrino transport and hydrodynamics allows us to take into account changes of the neutrino emission and of the associated postshock neutrino heating that are caused by rotational effects. For example, rapid rotation has consequences for the structure of the neutron star (e.g., it leads to centrifugal deformation), for the convective activity inside of the neutron star (because steep angular momentum gradients can suppress convection; see Buras et al. 2006a; Dessart et al. 2006), and for the mass flow through the postshock layer onto the nascent neutron star (since, e.g., SASI sloshing and spiral modes affect the dynamics of the postshock region and trigger shock expansion). All of these phenomena lead to modifications of the radiated neutrino luminosities and spectra and to corresponding directional variations, which are not accounted for in simple light-bulb treatments. Employing a pre-collapse angular momentum distribution from a stellar evolution model defines an important reference point for the influence of rotation on the explosion in “realistic” stellar cores. Our results will demonstrate that all of these aspects, which reach beyond previous studies using neutrino light bulbs and parametrized initial rotation profiles, are relevant for assessing the importance of rotation in the neutrino-heating mechanism for driving SN explosions.

Similar to the correction factor accounting for turbulent pressure and thermal dissipation, we derive an additional term representing the effects of rotation (see also

Janka et al. 2016). This allows us to include our set of rotation models to the representation of the generalized critical condition introduced by Summa et al. (2016). In order to validate this criterion for an extended region in the $(L_\nu \langle E_\nu^2 \rangle)_{\text{corr}} - (\dot{M} M_{\text{NS}})^{3/5}$ -plane, we additionally present 2D and 3D simulations of more massive, black-hole forming progenitors. These models from a forthcoming paper (Summa et al., in prep.) possess higher values of the “heating functional” $L_\nu \langle E_\nu^2 \rangle$, as well as larger values for the mass-accretion rate \dot{M} and neutron star mass M_{NS} . With the large set of 2D and 3D models

at hand, we show that the generalized critical condition provides an excellent criterion to separate models with failed shock expansion from those with successful shock revival.

The paper is structured as follows. After a brief description of the numerical setup in Sect. 2, our simulation results are presented in Sect. 3. In Sect. 4, we place our model set within the context of the generalized critical luminosity condition introduced by Summa et al. (2016) and conclude in Sect. 5.

Table 1. Overview of 2D and 3D simulations

model	dimension	rotation	angular resolution	explosion time ^a	end of simulation
m15_3D_artrot_2deg	3D	fast	2 degrees	0.217 s	0.460 s
m15_3D_rot_2deg	3D	Heger et al. (2005)	2 degrees	-	0.368 s
m15_3D_rot_6deg	3D	Heger et al. (2005)	6 degrees	-	0.453 s
m15_3D_norot_4deg	3D	no	4 degrees	-	0.329 s
m15_3D_norot_6deg	3D	no	6 degrees	-	0.377 s
m15_2D_artrot_1.4deg	2D	fast	1.4 degrees	-	0.434 s
m15_2D_artrot_2deg	2D	fast	2 degrees	-	0.476 s
m15_2D_rot_1.4deg	2D	Heger et al. (2005)	1.4 degrees	0.398 s	0.521 s
m15_2D_rot_2deg	2D	Heger et al. (2005)	2 degrees	0.416 s	0.500 s
m15_2D_norot_1.4deg	2D	no	1.4 degrees	0.454 s	0.567 s
m15_2D_norot_2deg	2D	no	2 degrees	0.513 s	0.626 s

^aOnset of explosion defined by the point in time when the ratio of advection to heating time scale reaches unity.

2. NUMERICAL SETUP

The calculations presented in this paper were performed with the neutrino-hydrodynamics code PROMETHEUS-VERTEX. This tool couples the hydrodynamics solver PROMETHEUS (Fryxell et al. 1989) via lepton number, energy, and momentum source terms with the neutrino transport module VERTEX (Rampp & Janka 2002). Applying three-flavor, energy-dependent, ray-by-ray-plus (RbR+) neutrino transport (see Buras et al. 2006b), VERTEX includes the full set of neutrino reactions and microphysics currently available (cf. Marek & Janka 2009; Müller et al. 2012). At high energies, the equation of state (EoS) of Lattimer & Swesty (1991) with a nuclear incompressibility of 220 MeV was used. We applied a low-density EoS with 23 nuclear species for nuclear statistical equilibrium (NSE) in regions with temperatures/densities above/below a certain threshold value which was chosen differently before and after bounce. Below NSE temperature, we used the flashing treatment as an approximation for nuclear burning (cf.

Rampp & Janka 2002). The simulations were conducted with a 1D gravitational potential including general relativistic corrections as described for Case A in Marek et al. (2006). Since rotational deformation of the proto-neutron star can only be observed at late times for the fastest rotating progenitor model of this study (see discussion below), the application of a 1D potential as well as the RbR+ method is reasonably well justified to follow our models during the post-bounce accretion phase towards the onset of explosion.

For all simulations, we used the (spherically symmetric) $15 M_\odot$ progenitor model m15u6¹ from the stellar evolution calculations of Heger et al. (2005), which include angular momentum transport by magnetic fields. Up to 10 ms after bounce, all models were computed on a spherical polar grid in 2D with initially 400 radial and 96 or 128 angular zones (denoted with “2deg”

¹ <http://www.2sn.org/stellarevolution/magnet/>

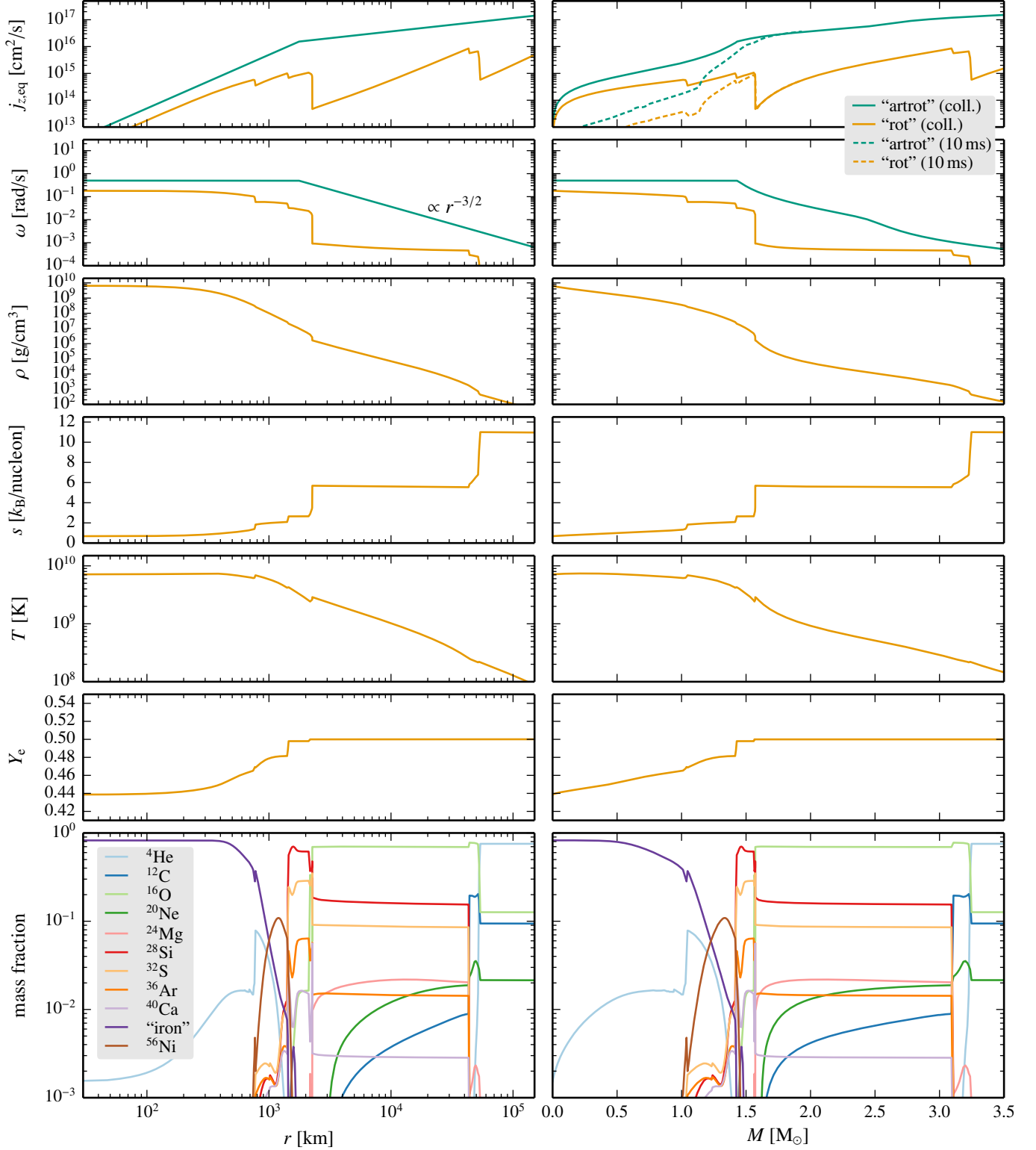


Figure 1. Initial profiles of angular momentum, angular velocity, density, entropy, temperature, electron fraction, and nuclear mass fractions (from top to bottom) versus radius (left column) and mass (right column) as given by the 1D stellar evolution calculations of Heger et al. (2005) for their model m15u6 at the onset of collapse (case “rot”). In addition, the enhanced angular momenta and velocities for our “artrot” case are shown (green lines in the top four panels). The difference between initial (i.e., pre-collapse; lines denoted by “coll.” in the legend box) and 10 ms-post-bounce values (dashed lines in the upper right panel; cases denoted by “10 ms” in the legend box) visualizes our erroneous loss of angular momentum during the collapse phase (see Sect. 2). For the mass fractions, the notation “iron” refers to the sum of neutron-rich isotopes in the iron group, in particular ^{54}Fe , ^{56}Fe , and ^{58}Fe .

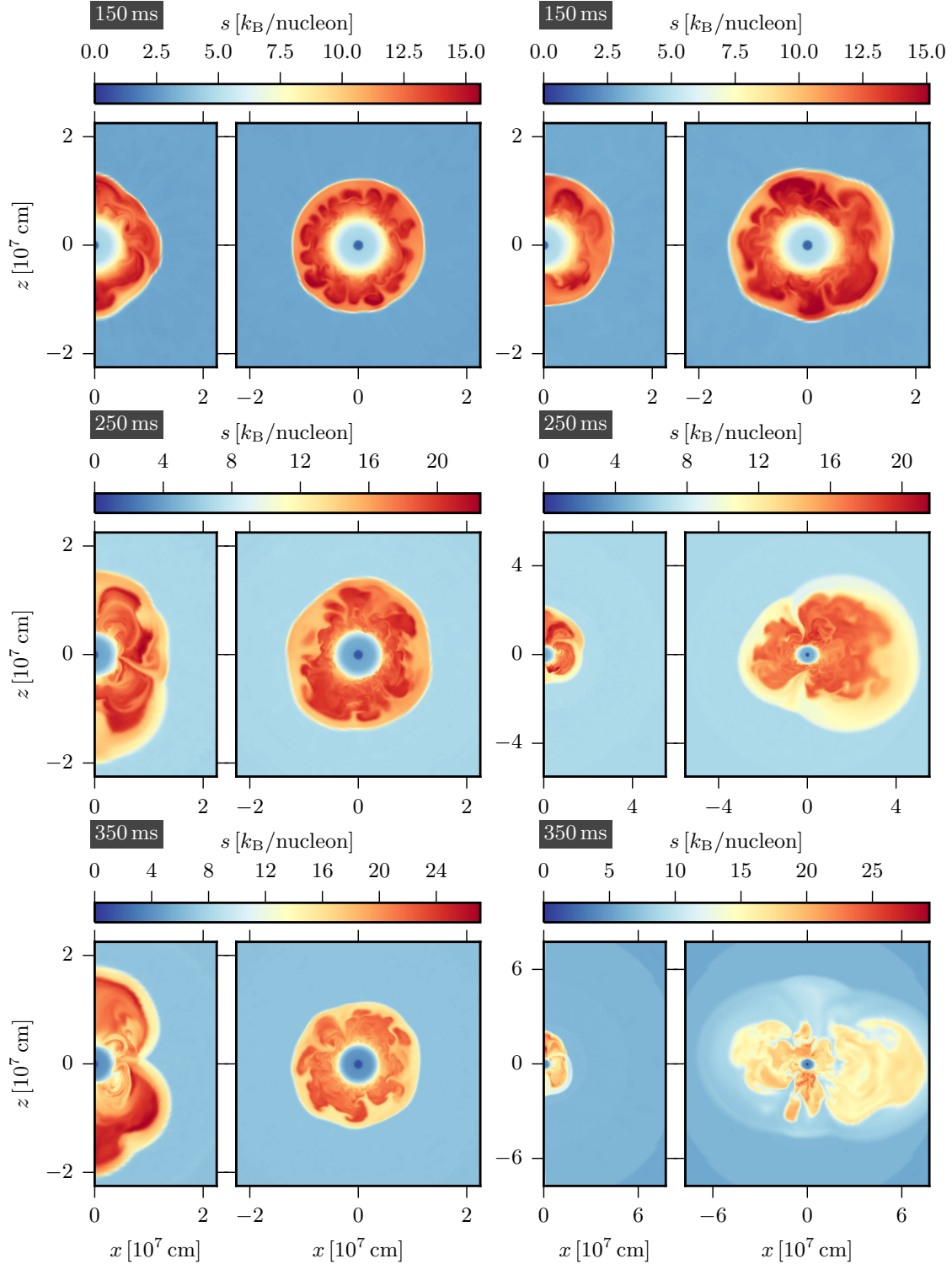


Figure 2. Snapshots of entropy for simulations with moderate (left column, exploding model m15_2D_rot_2deg and nonexploding model m15_3D_rot_2deg) and fast rotation (right column, nonexploding model m15_2D_artrot_2deg and exploding model m15_3D_artrot_2deg). From top to bottom, cross-sectional cuts in the x - z -plane (the z -axis coincides with the rotation axis of the progenitor model) at 150 ms, 250 ms, and 350 ms after core bounce are shown. In the left panels, the 2D models are depicted, the 3D simulations are displayed in the right panels. Note the changing scales of the plots in the right column.

or “1.4deg” in the model name). Computing the infall phase until 10 ms post bounce in 3D is not necessary. The reason is that triaxial instabilities are not expected to occur until this time for the moderately fast pre-collapse rotation associated with the angular momentum profiles adopted for this work. Indeed, our simulations confirmed that the first hydrodynamical flows with relevant 3D effects do not develop before 100 ms after bounce. We considered two cases for the initial rotation profiles that are indicated in the model names: While the abbreviation “rot” denotes simulations using the initial angular velocities given by [Heger et al. \(2005\)](#) (corresponding to an equatorial rotation velocity of 300 km s^{-1} on the zero-age main sequence), simulations with the designation “artrot” employed a rotation profile that was already used in previous publications by [Müller et al. \(2004\)](#); [Buras et al. \(2006b\)](#); [Marek & Janka \(2009\)](#). Besides allowing us to refer to our experience with the previous calculations, this profile, as before, was chosen to approximately reproduce the overall trends of pre-collapse models found in stellar evolution models with rotation, namely a roughly rigidly rotating iron core surrounded by shells with radially decreasing angular velocity but increasing angular momentum for a rotationally stable stratification. Moreover, the adopted “artrot” profile maximizes rotational effects but at the same time avoids sub-millisecond periods of the forming proto-neutron star. Furthermore, our choice guarantees that the rotational deformation of the stellar core is negligible at early times after bounce (see [Müller et al. 2004](#)). For comparison, both initial angular velocity profiles at the beginning of collapse are shown in [Fig. 1](#). In both cases, the angular velocity was assumed to be constant on spheres.

Because of an accidental mistreatment of fictitious forces in the 2D simulations up to 10 ms after bounce², the angular momentum of the infalling material is initially not exactly conserved. This leads to slower rotation frequencies of shells that have collapsed significantly up to core bounce and a corresponding reduction of the angular momentum mostly of matter that gets integrated into the proto-neutron star during the later accretion (see also [Fig. 1](#)). However, because this deficit only holds for the initial collapse phase in 2D and hardly affects the material accreted at times later than 100 ms of post-bounce evolution, it is not crucial for our discussion of the angular momentum evolution of the gain region and the resulting effects on the explosion physics (see [Sect. 3](#)).

The growth of aspherical instabilities was seeded by

randomly imposed cell-to-cell perturbations of 0.1% in radial velocity on the entire computational grid at the beginning of the simulation. In the case of the 3D simulations, at 10 ms after bounce the data were mapped to an axis-free Yin-Yang grid ([Kageyama & Sato 2004](#); [Wongwathanarat et al. 2010](#)) with an angular resolution as given in the model name. In order to avoid excessive time step limitations at the grid center, the innermost 1.6 km of the stellar core were treated in spherical symmetry. The zones of the radial grid were non-equidistantly distributed from the center with a reflecting boundary at the coordinate origin to an outer boundary of 10^9 cm with an inflow condition. During the simulations, the radial grid was gradually refined, reaching a number of ~ 600 zones and a resolution of $\Delta r/r \sim 3.5 \times 10^{-3}$ at the gain radius at the time the simulations were stopped. For the neutrino transport, 12 geometrically spaced energy bins with an upper bound of 380 MeV were employed.

For one 3D simulation up to $\sim 0.5 \text{ s}$ after bounce with an angular resolution of two degrees (e.g. model `m15.3D_artrot.2deg`), the computational costs amounted to roughly 50 million CPU hours on, for example, *Sandy Bridge-EP Xeon E5-2680 8C* processors on SuperMUC of the Leibniz Supercomputing Centre (LRZ). Typically, roughly 16,000 cores were employed in parallel. For the whole model set, the computational costs summed up to about 130 million CPU hours.

3. RESULTS AND DISCUSSION

In this section, we present the results of our 2D and 3D CCSN simulations of rotating progenitor stars. After a short overview of the complete model set and a comparison between rotational effects in 2D and in 3D, we focus on our two best resolved 3D models with moderate and enhanced rotation rates and discuss the influence of rotation on the explosion physics in detail.

3.1. General Properties of Rotation-supported Models in 2D and 3D

In [Fig. 3](#), the time evolution of the mean shock radius is given for the whole set of five 3D and six 2D models. [Table 1](#) provides an overview of the computed 2D and 3D models. The 3D model set consists of a fast rotating model (angular resolution of 2 degrees, for more details see [Sect. 2](#)), two moderately rotating models (angular resolutions of 2 and 6 degrees), and two nonrotating models (4 and 6 degrees). Only the fast rotating model `m15.3D_artrot.2deg` develops an explosion, all other 3D models do not explode before the simulations are stopped. The larger shock radii of the less resolved models between 0.2 and 0.3 s after bounce compared to model `m15.3D_rot.2deg` are due to a more pronounced activity of the standing accretion-shock insta-

² Several code lines had been deactivated for test calculations and reactivation had been forgotten afterwards.

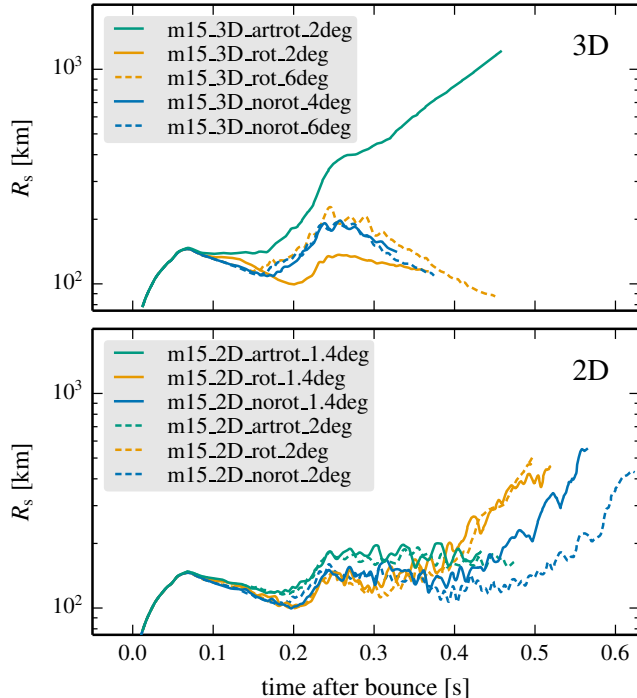


Figure 3. Time evolution of shock radius (averaged over all angular directions) for our simulations in 3D (upper panel) and in 2D (lower panel). The curves are smoothed by running averages of 5 ms.

bility (SASI), which is not strongly present in the better resolved model with a moderate rotation rate (see also Sect. 3.4). In the models with angular cell sizes of 4 or 6 degrees, turbulent eddies due to convection cannot be resolved on small scales and the growth of SASI modes seems to be facilitated by the suppression of parasitic Rayleigh-Taylor and Kelvin-Helmholtz instabilities. This is why we will focus on the 2-degree-runs in the discussion of the results and will only depict the results of the three best-resolved 3D simulations in all subsequent figures.

The 2D model set consists of six models with angular resolutions of 1.4 and 2 degrees for each of the three different (fast, moderately, and nonrotating) cases. Since the time evolution of the better resolved models is very similar to the models with an angular resolution of 2 degrees, only the latter ones are presented in the following figures. This places the 2D and 3D simulations on (roughly) equal footing with respect to resolution.

Compared to their 3D counterparts, the behavior of the 2D models is different (see Figs. 2 and 3). While the moderately and nonrotating 2D models explode, the fast rotating 2D model does not evolve towards a successful explosion before the end of the simulation. This distinct behavior underlines the need for simulations in three dimensions to assess the effects of rotation in the context of the neutrino-driven explosion mechanism.

A comparison of the neutrino luminosities and mean

energies (see Fig. 4) shows only minor differences between the 2D (dashed lines) and 3D models (solid lines). While the effect of moderate rotation rates on the neutrino quantities is negligible (compare models m15_2D_rot_2deg and m15_3D_rot_2deg to the nonrotating cases), the influence of rotation is clearly visible in models m15_2D_artrot_2deg and m15_3D_artrot_2deg. After 100 ms post bounce, neutrino luminosities and mean energies are significantly reduced due to the more extended and cooler rotating neutron star (see Fig. 5 and Buras et al. 2006b; Marek & Janka 2009). In the 3D model the effect is even stronger than in the corresponding 2D case due to the growth of the shock stagnation radius, which reduces the mass-accretion rate of the neutron star (see Fig. 5 for a slower growth of the neutron star mass) and its ν_e and $\bar{\nu}_e$ emission, in particular, since energy is stored in rotation associated with spiral SASI mass motions instead of being released by neutrinos.

Therefore, the neutrino heating rate per unit mass, $\dot{Q}_{\text{heat}}/M_g$, is considerably lower than in the moderately and nonrotating models (see Fig. 6). Here, the neutrino heating rate is defined as the integral of the net neutrino energy deposition rate per volume q_e (heating minus cooling) over the gain layer,

$$\dot{Q}_{\text{heat}} = \int_{V_g} q_e dV, \quad (1)$$

and M_g is given by the mass enclosed in the gain layer,

$$M_g = \int_{V_g} \rho dV. \quad (2)$$

Because shock expansion is supported by the spiral SASI mode in model m15_3D_artrot_2deg, the mass in the gain layer grows and overcompensates for the decrease of the specific heating rate. For this reason the heating rate \dot{Q}_{heat} and the heating efficiency, defined by the ratio of the total energy deposition rate to the sum of the radiated electron neutrino and electron antineutrino luminosities,

$$\eta = \frac{\dot{Q}_{\text{heat}}}{L_{\nu_e} + L_{\bar{\nu}_e}}, \quad (3)$$

are even highest in model m15_3D_artrot_2deg (see Figs. 6 and 7).

This also leads to a longer neutrino heating time scale (see Fig. 8),

$$\tau_{\text{heat}} = \frac{|E_{\text{tot,g}}|}{\dot{Q}_{\text{heat}}}, \quad (4)$$

where $E_{\text{tot,g}}$ is the total (i.e., internal plus kinetic (including rotational) plus gravitational) energy in the gain layer. Due to the larger mass contained in the gain layer, the value of the total energy is lower (more negative),

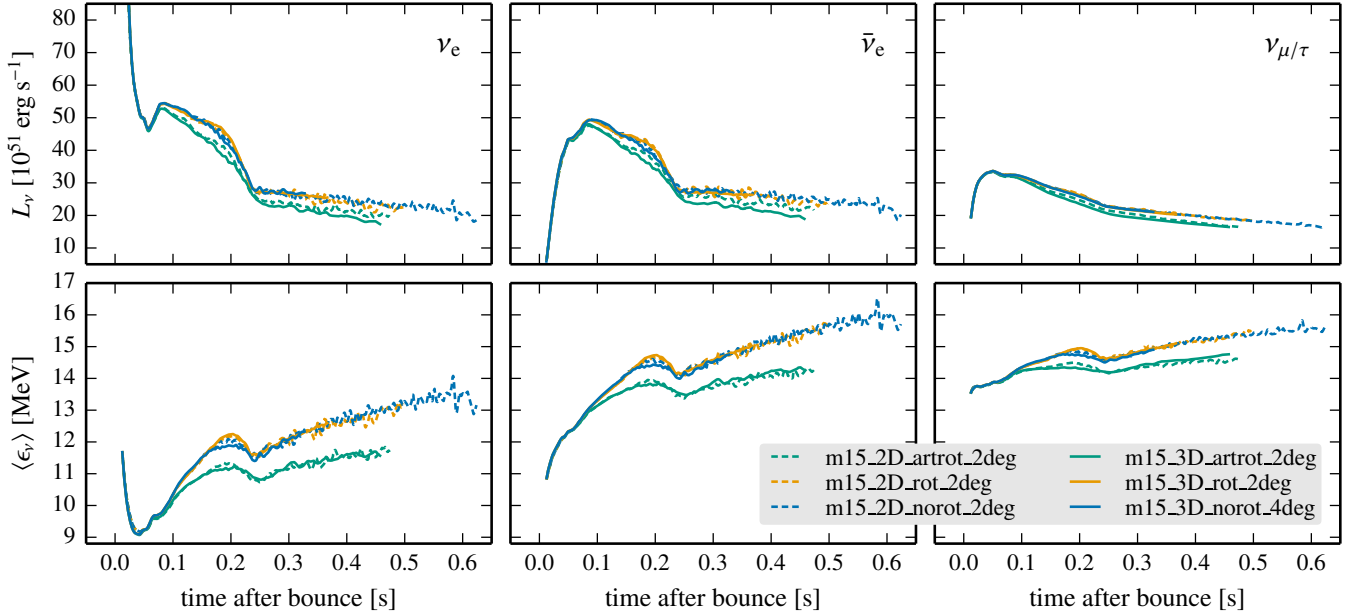


Figure 4. Time evolution of neutrino luminosities (first row) and neutrino mean energies (ratio of neutrino energy flux to neutrino number flux; second row) for the simulations in 2D (dashed lines) and in 3D (solid lines; lab-frame quantities, evaluated at 400 km and given for an observer at infinity). From left to right, the angular averages are shown for ν_e , $\bar{\nu}_e$, and ν_μ/τ . The curves are smoothed by running averages of 5 ms.

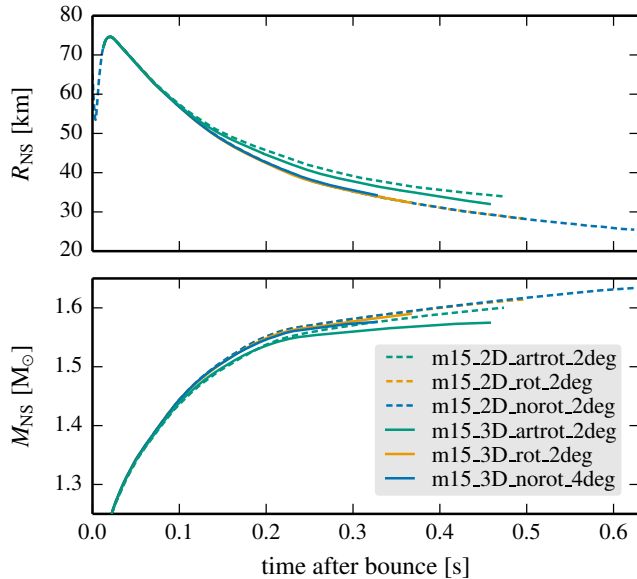


Figure 5. Time evolution of the average neutron star radius (upper panel) and baryonic neutron star mass (lower panel). Both quantities are defined by the radius where the density is $10^{11} \text{ g cm}^{-3}$ on the angle-averaged density profile. The curves are smoothed by running averages of 5 ms.

but the specific total energy in the gain layer is significantly higher than in the other models because of the additional kinetic energy provided by the spiral SASI mode (see Fig. 7).

In 2D, however, all models show roughly the same time-scale ratio $\tau_{\text{adv}}/\tau_{\text{heat}}$ until models m15_2D_norot_2deg and m15_2D_rot_2deg finally explode. In the fast rotating model m15_2D_artrot_2deg,

centrifugal forces stabilize the accretion shock at larger radii (see Fig. 3 and Fig. 6, upper panel) and increase the advection time scale noticeably (compare the advection time scales of all 2D models (dashed lines) between 200 and 400 ms after bounce in Fig. 8, second panel from top). Here, the advection time scale is defined by the dwell time of matter in the gain region (cf. Buras et al. 2006a; Marek & Janka 2009):

$$\tau_{\text{adv}} \equiv \tau_{\text{dwell}} \approx \frac{M_{\text{g}}}{\dot{M}}, \quad (5)$$

where \dot{M} is the mass-accretion rate through the shock. But this favorable influence of rotation on the explosion conditions cannot overrule the reduced energy deposition by neutrinos due to the lower neutrino luminosities and mean energies in model m15_2D_artrot_2deg. Different from model m15_2D_rot_2deg and model m15_2D_norot_2deg, this fast rotating model does not explode until the simulation is stopped.

In contrast, in 3D *only* the setup with the fastest rotation (model m15_3D_artrot_2deg) develops an explosion. The nonrotating 3D case (model m15_3D_norot_4deg) does not explode although it exhibits a more favorable time-scale ratio (see Fig. 8) than the exploding nonrotating and rotating 2D models m15_2D_norot_2deg and m15_2D_rot_2deg. This finding is consistent with previous results for nonrotating 11.2, 20, and 27 M_{\odot} progenitors, which also did not explode in 3D whereas their 2D counterparts did (see Hanke et al. 2013; Tamborra et al. 2014b,a).

The fast rotating model m15_3D_artrot_2deg shows

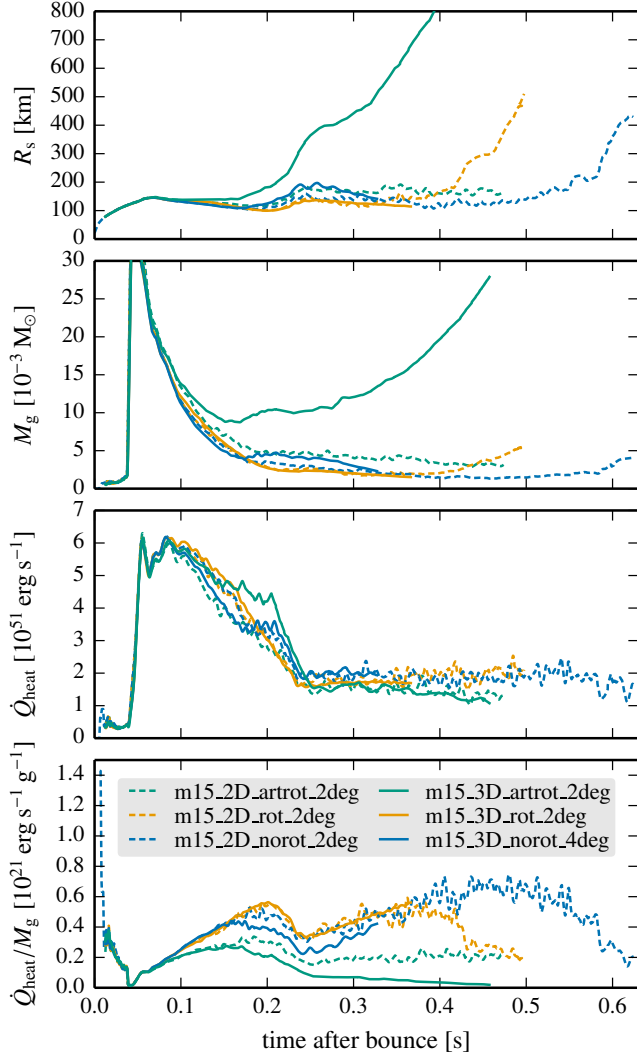


Figure 6. Time evolution of average shock radius, gain layer mass, neutrino heating rate, and neutrino heating rate per unit mass in the gain layer (from top to bottom). The curves are smoothed by running averages of 5 ms.

the largest values of the advection time scale shortly after bounce. This is caused by the early development of a strong spiral SASI mode, which immediately drives the shock to larger radii and leads to a strong increase of the nonradial kinetic energy and the mass contained in the gain layer. This SASI spiral mode therefore has a much larger influence than SASI sloshing motions in model m15_2D_artrot_2deg (compare both models in Fig. 6). The explosion properties of these fast rotating models will be further discussed in Sect. 3.4.

3.2. Angular Momentum Evolution

The strong spiral SASI mode in model m15_3D_artrot_2deg also leaves its imprint on the angular momentum profiles: Compared to the 2D case, the angular velocities in the gain region are significantly increased (see lower left panels of Figs. 9 and 10).

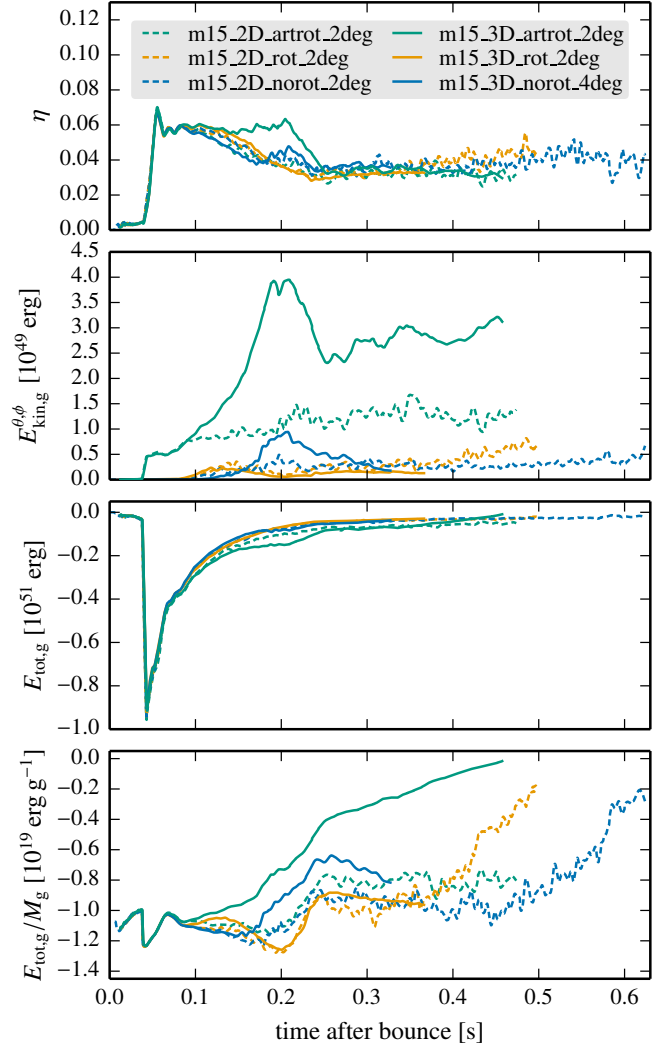


Figure 7. Time evolution of neutrino heating efficiency, kinetic energy of nonradial motions, total energy, and total specific energy in the gain layer (from top to bottom). The curves are smoothed by running averages of 5 ms.

Prominent spikes due to spiral-SASI activity can be seen in model m15_3D_artrot_2deg at $M \approx 1.5 M_\odot$ for $t = 150$ ms and at $M \approx 1.6 M_\odot$ for $t = 300$ ms (see lower left panel of Fig. 10). Such a pronounced 2D-3D difference cannot be observed in the slow-rotating cases. Due to the strong decline of the angular velocities at the Si/Si-O interface (see the sudden drop at a radius of ~ 2000 km in Fig. 1), the angular momentum contained in the gain layer decreases at later times (compare profiles for $r \gtrsim 50$ km at later and earlier times). While in 2D the specific angular momentum of each mass element is preserved, in 3D the initially uniform, uni-directional rotation pattern is destroyed by convective and turbulent motions, i.e. the rotation rates of the accreted material are too low to dominate the fluid motions associated with hydrodynamic instabilities in the gain region in a global way (see

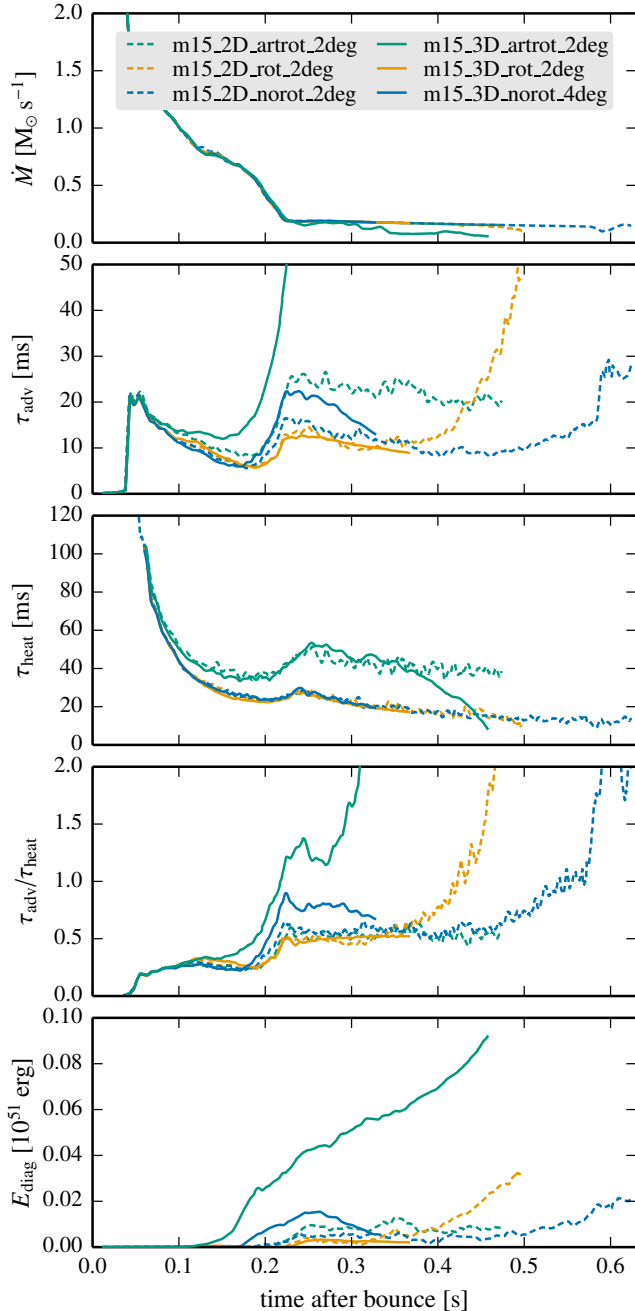


Figure 8. Time evolution of mass-accretion rate (evaluated at a radius of 400 km), advection and heating time scale in the gain layer as well as the ratio of the two time scales, and diagnostic explosion energy (from top to bottom). The curves are smoothed by running averages of 5 ms.

the angular momentum profile at 300 ms for model m15_3D_rot_2deg in Fig. 10).

A comparison of the angular momentum contained in the neutron star in 2D and 3D (the z -axis is the rotation axis) is given in Fig. 11 for the moderately and fast rotating cases. Angular momentum is naturally conserved in axisymmetry. Model m15_2D_rot_2deg exhibits only a slow growth when low-angular momentum material from

outside the Si/Si-O interface is accreted, whereas $J_{z,\text{NS}}$ for the more rapidly rotating model m15_2D_artrot_2deg continues to increase as the neutron star mass grows with time by the infall of high- j_z matter (Fig. 5). In contrast, the 3D simulations show noticeable angular momentum losses towards later post-bounce times. Most of this effect is caused by the applied numerical schemes which guarantee momentum and energy conservation, but do not conserve angular momentum up to machine precision. Especially at early times in the linear regime of SASI growth, these losses are negligible and do not influence the interaction between rotation and the development of SASI.

A smaller part of the effect may be associated by the redistribution of low-angular momentum material into the neutron star (defined by $\rho \geq 10^{11} \text{ g cm}^{-3}$) due to nonspherical flows around the neutron star, while high- j_z matter stays outside of the neutron star when the explosion sets in in model m15_3D_artrot_2deg. Inside of the proto-neutron star, in 2D as well as in 3D, angular momentum is redistributed by convective mass motions in the convective shell below the neutrinosphere. For this reason the radial profile of the specific angular momentum (j_z) versus mass in the region $M \lesssim 1.5 M_{\odot}$ cannot be expected to be preserved (see right columns of Figs. 9 and 10).

The fact that the angular momentum of the neutron star is roughly one order of magnitude larger in the fast rotating models directly translates into higher expected pulsar rotation rates. Assuming angular momentum conservation, a final neutron star radius of 12 km, a moment of inertia of $0.35 M_{\text{grav}} R_{\text{NS}}^2$ (cf. Lattimer & Prakash 2001) and taking the respective final values of the two 3D simulations into consideration, the final neutron star spin period evaluates to 5 ms for model m15_3D_artrot_2deg and to 66 ms for model m15_2D_artrot_2deg. Note that the latter value is larger than the one derived in Heger et al. (2005) because of the erroneous angular momentum loss in our simulations during the collapse phase, which leads to a reduction of the angular momentum content in the inner core (see Sect. 2 and Figs. 1, 9, and 10).

3.3. Turbulent Energy Cascades

In order to study the turbulent energy cascades in our models, we consider the energy spectrum $E(l)$ of turbulent motions as a function of multipole order l at a chosen radius in the gain region by using a decomposition of the nonradial velocity field into spherical harmonics $Y_{lm}(\theta, \phi)$ (cf. Hanke et al. 2012; Summa et al. 2016):

$$E(l) = \sum_{m=-l}^l \left| \int_{\Omega} Y_{lm}^*(\theta, \phi) \sqrt{\rho} v_{\text{ang}}(r, \theta, \phi) d\Omega \right|^2, \quad (6)$$

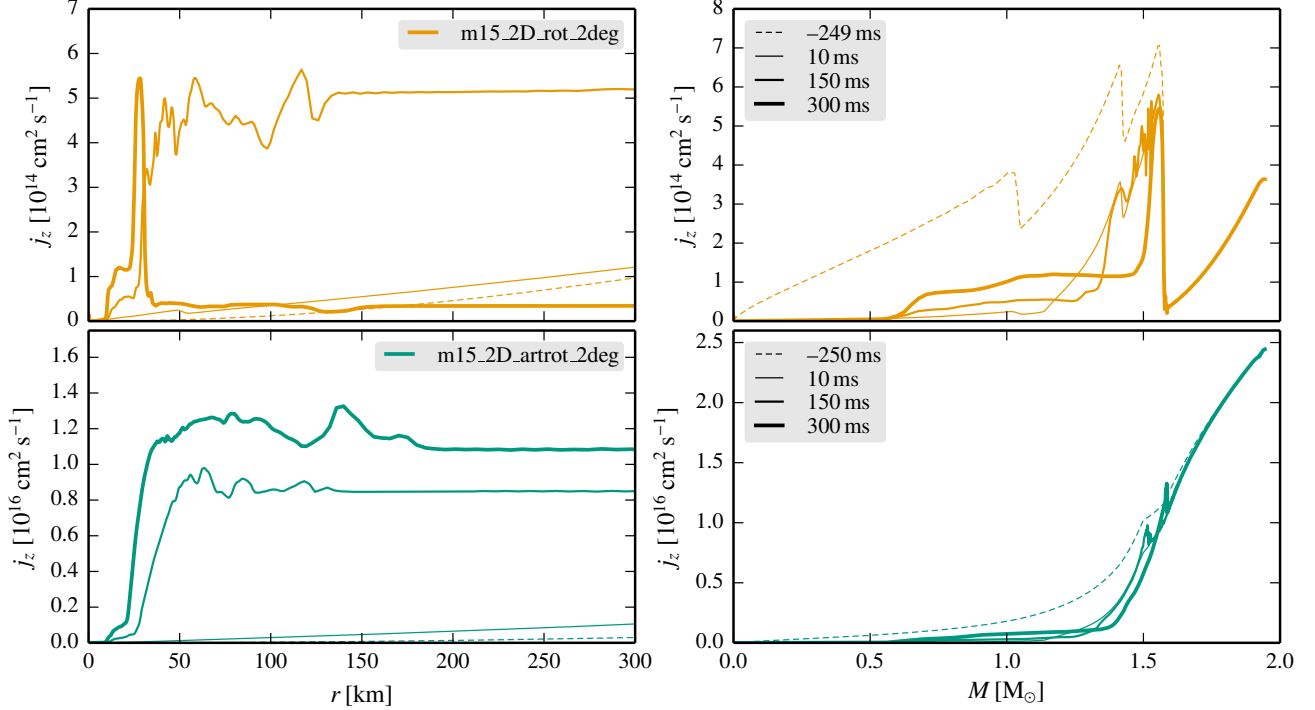


Figure 9. Time evolution of angular momentum profiles vs. radius (left) and enclosed mass (right) for the moderately (upper row) and fast rotating cases (lower row) in 2D. The enclosed mass M is defined as the mass encompassed by spheres of growing radius (and is therefore not an ideal Lagrangian coordinate). The specific angular momentum j_z is computed as the ratio of the z -component of the angular momentum in spherical shells divided by the mass of the shells. Note that an accidental mistreatment of fictitious forces in the simulation code up to 10 ms after bounce leads to a temporary violation of angular momentum conservation, but this only affects the final neutron star spins.

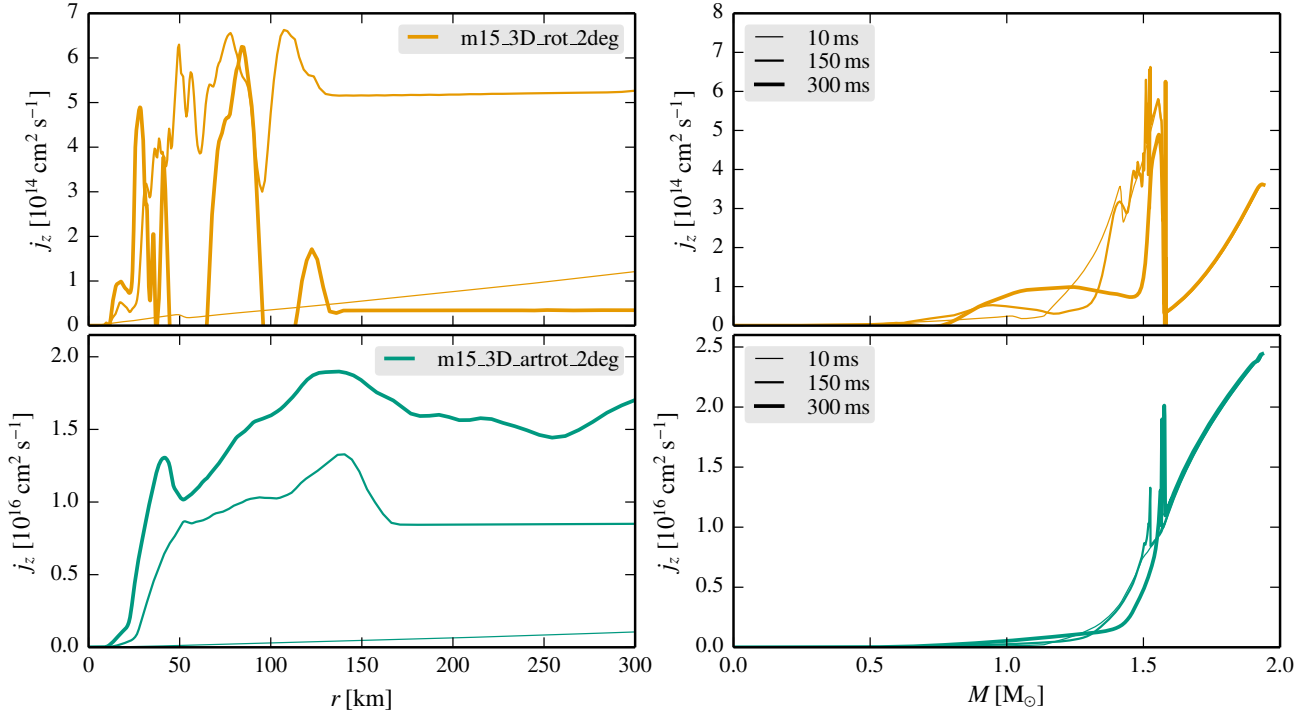


Figure 10. Time evolution of angular momentum profiles vs. radius (left) and enclosed mass (right) for the moderately (upper row) and fast rotating cases (lower row) in 3D. Definition of quantities analogous to Fig. 9.

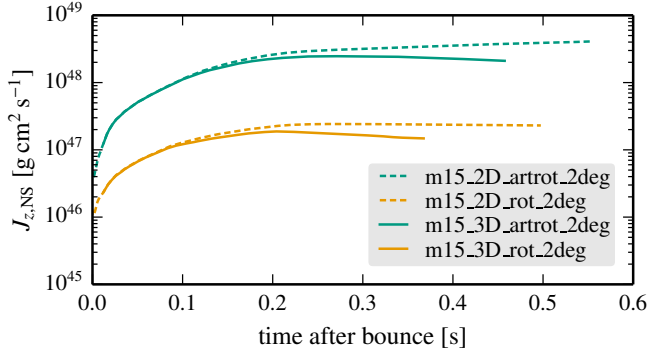


Figure 11. Time evolution of the z -component of the angular momentum of the neutron star. The latter is defined by the mass at densities above $10^{11} \text{ g cm}^{-3}$ for an angle-averaged density distribution. The curves are smoothed by running averages of 5 ms.

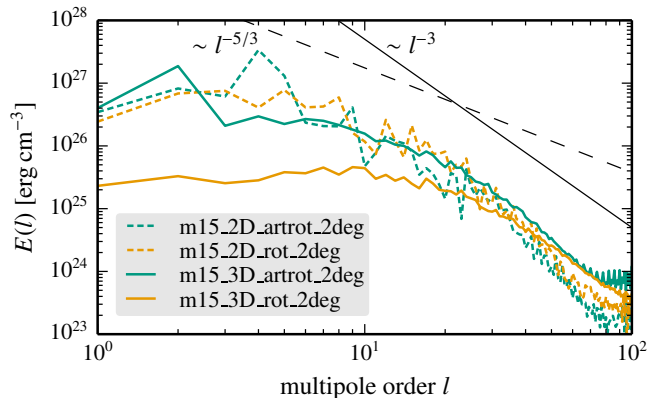


Figure 12. Turbulent energy spectra $E(l)$ as functions of the multipole order l for simulations in 3D (solid lines) and 2D (dashed lines). The spectra are based on a decomposition of the nonradial velocity components into spherical harmonics at 150 ms after bounce (before the onset of an explosion in model m15_3D_artrot_2deg), averaged over a time interval of 5 ms and a radius interval of 10 km around the midpoint between gain radius and minimum shock radius. The thin dashed and solid black lines indicate reference spectral slopes of $-5/3$ and -3 .

where $v_{\text{ang}} = \sqrt{v_{\theta}(r, \theta, \phi)^2 + v_{\phi}(r, \theta, \phi)^2}$. The results for the moderately and fast rotating 2D and 3D models are shown in Fig. 12.

Due to the inverse energy cascade in axisymmetry, the injected energy is not transferred to the dissipative range and $E(l) \propto l^{-5/3}$ approximately holds for $l \lesssim 30$ in models m15_2D_rot_2deg and m15_2D_artrot_2deg. At larger l , the direct vorticity cascade leads to a power-law index of ~ -3 (Kraichnan 1967; Hanke et al. 2012). Model m15_3D_rot_2deg develops a power-law spectrum following approximately $E(l) \propto l^{-5/3}$ at intermediate wavenumbers ($l \sim 20 - 50$), which is characteristic for the energy transfer in 3D from large to small scales up to the dissipation range at large l (Landau & Lifshitz 1959; Hanke et al. 2012).

In contrast to the forward energy cascade of model m15_3D_rot_2deg, model m15_3D_artrot_2deg exhibits an energy spectrum which is very similar to the axisymmetric case. This unusual behavior can be explained by the presence of fast rotation. While the rotational effects in the moderately rotating 3D model are not strong enough to affect the energy transport, the global fast rotation of model m15_3D_artrot_2deg leads to an anisotropic flow which approaches two-dimensionality due to the rotational constraints of the flow geometry in the azimuthal direction.

This phenomenon of rotational turbulence has also been studied in the context of geophysical and industrial flows and is subject to current research in these fields (see Smith & Waleffe 1999; Rubio et al. 2014; Godefert & Moisy 2015, and references therein). Depending on the Rossby number Ro being defined as the ratio of inertia force to Coriolis force (Godefert & Moisy 2015; Müller 2016),

$$Ro = \frac{U}{2\omega L} \sim \frac{|v_r|}{2(R_s - R_g)\omega} \sim \frac{R_s^2}{2\tau_{\text{adv}}j} \sim \frac{1}{4\pi} \frac{T_{\text{rot}}}{\tau_{\text{adv}}} \quad (7)$$

(U and L are characteristic velocity and length scales, R_g and R_s the mean gain and shock radius, and ω , j , and T_{rot} the average angular velocity, specific angular momentum, and rotation period of the infalling shells), different regimes of turbulent dynamics can be identified. For $Ro \gg 1$, turbulent flows evolve much faster than the rotation time scale and the turbulent structures are mostly unperturbed by rotation. This is the case for model m15_3D_rot_2deg with a Rossby number of ~ 20 in the gain layer at 150 ms after bounce. Only at low Ro , the rotation time scale is small enough for the Coriolis force to effectively influence the flow dynamics. This can be observed in model m15_3D_artrot_2deg where Ro evaluates to ~ 0.5 at 150 ms post bounce. The fact that the slopes of the energy spectra of the two 3D models become very similar for $l > 50$ (although one has to note that the regime of large l can suffer from resolution deficits) may be an indication that only large scales are affected by rotation in model m15_3D_artrot_2deg, while small scales below the Zeman scale (cf. Zeman 1994) still recover isotropic turbulence properties.

The clear trend of a “two-dimensionalization” of the flow in model m15_3D_artrot_2deg points towards an interesting feature of rotation in CCSN explosion models. Besides the additional amount of kinetic energy provided by rotation, also the turbulent energy cascade is (partially) reversed in the case of small Ro numbers. Similar to the behavior of 2D simulations (cf. Hanke et al. 2012), fast rotation in 3D supports the development of large-scale structures and the storage of energy on these scales, and therefore facilitates the evolution towards a successful explosion.

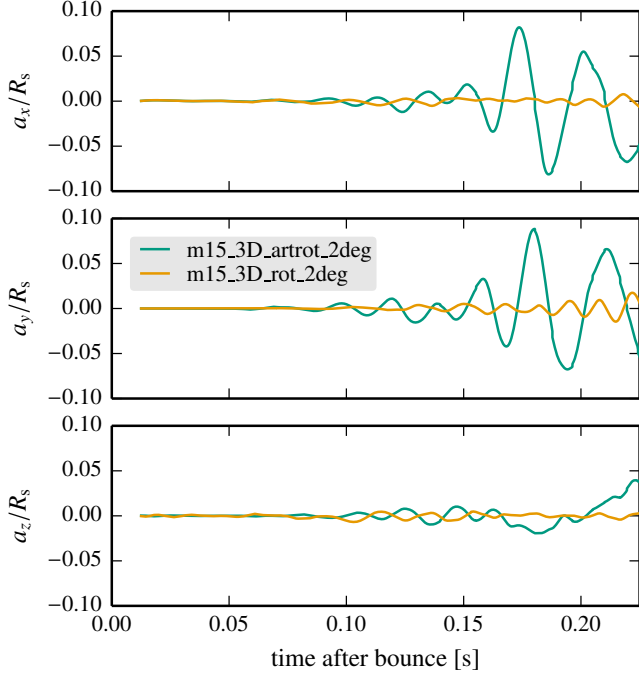


Figure 13. Time evolution of the coefficients a_x , a_y , and a_z for an expansion of the shock surface into spherical harmonics (see definition in Sect. 3.4). The coefficients are normalized to the $l = 0$, $m = 0$ mode (i.e. the average shock radius).

3.4. A Rotation-supported Supernova Explosion in 3D

The two best-resolved 3D models with moderate and enhanced rotation exhibit a largely different behavior: The fast rotating model m15_3D_artrot.2deg does not show any pronounced shock retraction phase and develops a strong spiral SASI mode giving support to a fairly early explosion even before the Si/Si-O interface reaches the shock (Figs. 1 and 8). In contrast, model m15_3D_rot.2deg is far away from a successful explosion and the ratio of advection and heating time scale never increases beyond a value of 0.5 (see Fig. 8).

We emphasize once more that this behavior of the 3D models with rotation is in strong discrepancy to the results for the corresponding 2D simulations. In 2D, slow rotation might tend to support the explosion, and model m15_2D_rot.2deg explodes somewhat earlier than the nonrotating case m15_2D_norot.2deg. However, our few models per case with a rather small difference in the explosion time are not sufficient to draw firm conclusions. Fast rotation in model m15_2D_artrot.2deg, however, delays the explosion (no success is obtained until the simulation was terminated at ~ 470 ms after bounce) because of the reduced energy deposition by neutrinos in the gain layer, which is a consequence of lower radiated neutrino luminosities and mean energies (Fig. 4). In the 3D model m15_3D_artrot.2deg the rotationally induced reduction of the emitted neutrino lu-

minosities and mean energies is even more pronounced, but this effect is overcompensated by the strong spiral SASI activity, which triggers the early explosion to set off in the equatorial plane.

The oblate deformation of the beginning 3D explosion, with accretion continuing along the polar directions, agrees with the results for even more rapidly spinning progenitor conditions by Nakamura et al. (2014) and Takiwaki et al. (2016) and is also in stark contrast to 2D explosions with and without rotation. In 2D, explosions start with a pronounced prolate deformation when the outgoing shock expands fastest along the polar direction, driven either by the SASI sloshing or stronger neutrino heating above the poles of the newly formed neutron star (see Fig. 2 and also Kotake et al. 2006).

In order to study the development of the SASI activity in a quantitative way, we perform a decomposition of the angle-dependent shock radius $R_s(\theta, \phi)$ into spherical harmonics Y_l^m :

$$a_l^m = \frac{(-1)^{|m|}}{\sqrt{4\pi(2l+1)}} \int_{\Omega} R_s(\theta, \phi) Y_l^m(\theta, \phi) d\Omega. \quad (8)$$

The orthonormal basis functions are given by

$$Y_l^m(\theta, \phi) = \sqrt{2} N_l^m P_l^m(\cos \theta) \cos(m\phi) \quad (9)$$

for $m > 0$, by

$$Y_l^m(\theta, \phi) = N_l^0 P_l^0(\cos \theta) \quad (10)$$

for $m = 0$, and by

$$Y_l^m(\theta, \phi) = \sqrt{2} N_l^{|m|} P_l^{|m|}(\cos \theta) \sin(|m|\phi) \quad (11)$$

for $m < 0$, with

$$N_l^m = \sqrt{\frac{(2l+1)(l-m)!}{4\pi(l+m)!}} \quad (12)$$

and $P_l^m(\cos \theta)$ being the associated Legendre polynomials (Burrows et al. 2012; Ott et al. 2013). With this choice of basis functions, the coefficients with $l = 1$ represent the angle-averaged Cartesian coordinates of the shock surface,

$$a_1^1 = \langle x_s \rangle \equiv a_x, \quad (13)$$

$$a_1^{-1} = \langle y_s \rangle \equiv a_y, \quad (14)$$

$$a_1^0 = \langle z_s \rangle \equiv a_z. \quad (15)$$

The time evolution of the SASI amplitudes can be inferred from Fig. 13. Although weak oscillations of the shock surface also arise in the case of model m15_3D_rot.2deg at 100 ms after bounce, a further growth of the amplitudes seems to be suppressed and the fluid motions in the gain layer are dominated by

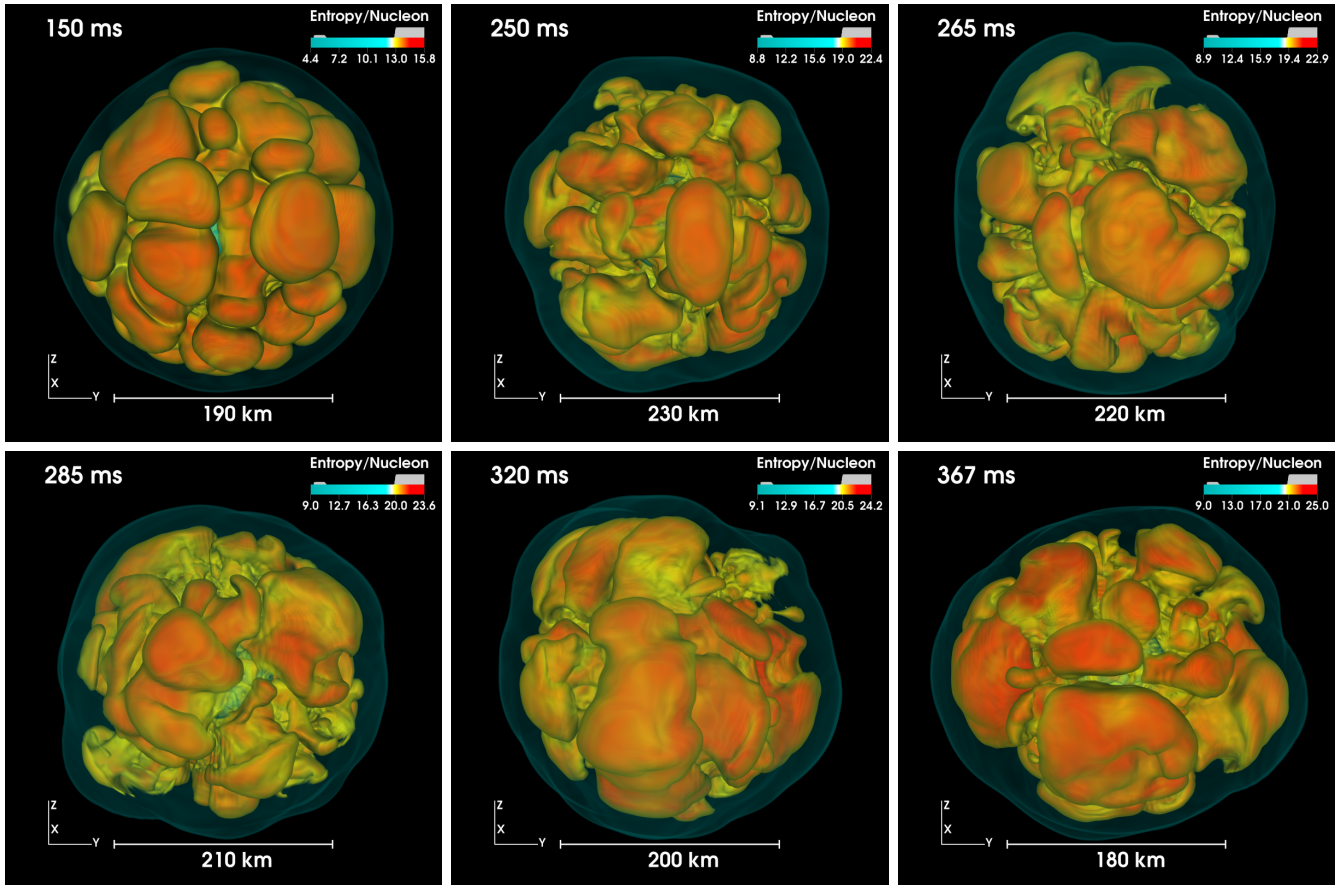


Figure 14. Volume rendered images of the nonexploding model `m15_3D_rot_2deg` for different times after bounce. The rotation axis of the progenitor is in the z -direction. Colors represent entropy in k_B per nucleon, the yardstick indicates the length scale. The supernova shock is visible by a thin bluish surface surrounding the high-entropy bubbles of neutrino-heated matter. The model is clearly convection dominated with only weak SASI activity.

convection (see also Fig. 14). While the advection time scales in both models are similar only at very early post-bounce times (cf. Fig. 8, second panel from top), model `m15_3D_artrot_2deg` first shows influence by the accumulating rotational energy in the gain layer and then exhibits a strong growth of a spiral SASI mode in the x - y -plane, which is perpendicular to the rotation axis of the infalling matter. The SASI motions drive the shock to larger and larger radii in the equatorial region and develop an oblate ejecta deformation (see Fig. 15). At later times, we observe the presence of a corotation radius (cf. Kazeroni et al. 2017), which means there is a location between neutron star and shock where the flow rotates faster than the SASI spiral pattern of the shock. Since the initial angular velocities are not as extreme as the rapid rotation rates assumed by Takiwaki et al. (2016), no one-armed spiral wave pattern emerges. Model `m15_3D_artrot_2deg` resembles an intermediate case situated between the two models presented in figure 4 of Kazeroni et al. (2017): The initially SASI-dominated rotation dynamics transitions to a phase where the innermost part of the gain region ro-

tates faster than the spiral SASI pattern, even though a tightly-wound spiral flow being characteristic for a pronounced corotational instability does not appear.

Due to the tremendous computational costs for 3D simulations with state-of-the-art neutrino transport, we cannot investigate the impact of rotation on the development of SASI for an extended set of models similar to the study by Kazeroni et al. (2017), who used largely simplified simulation setups. Especially in view of the stochastic nature of the SASI (cf. Kazeroni et al. 2017), the limited 3D model set presented in this paper does not allow any comprehensive evaluation of the impact of rotation on the growth of the SASI. But the fact that, on the one hand, no spiral SASI mode is triggered in the slowly rotating model `m15_3D_rot_2deg` and, on the other hand, a *sloshing* SASI mode emerges in its less-resolved counterpart `m15_3D_rot_6deg` (see the large excursions of the average shock radius of this model in Fig. 3), strongly suggests that the rotation rates obtained in current stellar evolution calculations including magnetic fields are not high enough to modify the explosion physics in a significant way compared to nonrotating progenitors.

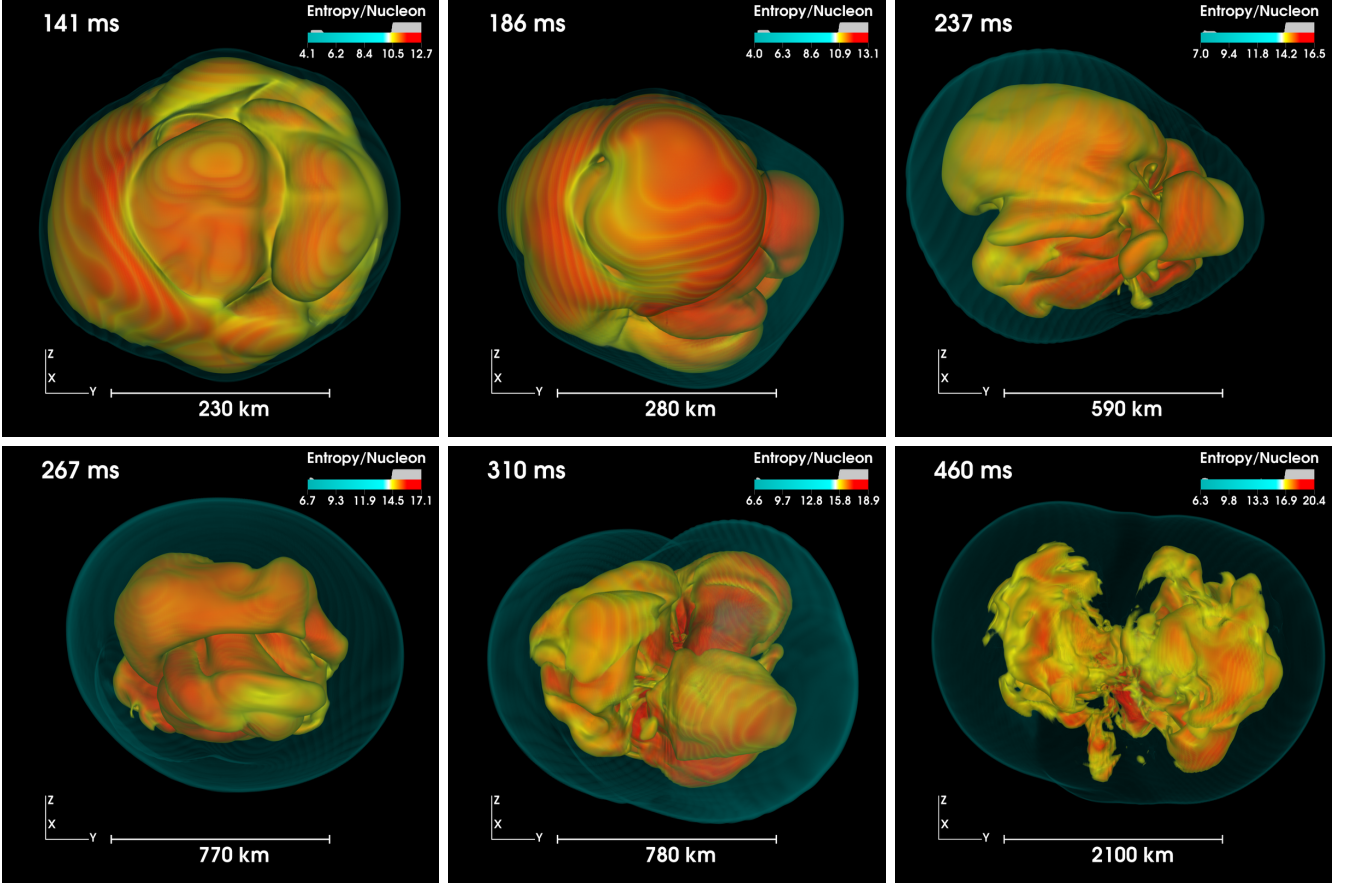


Figure 15. Volume rendered images of the exploding model `m15_3D_artrot_2deg` for different times after bounce. The rotation axis of the progenitor is the z -direction. Colors represent entropy in k_B per nucleon, the yardstick indicates the length scale. The supernova shock is visible by a thin bluish surface surrounding the high-entropy bubbles of neutrino-heated matter. The dynamics of the postshock layer are strongly dominated by a SASI spiral mode that supports an oblate-shaped explosion pushing the shock out in the equatorial plane perpendicular to the rotation axis of the progenitor model.

This conclusion is further supported by a comparison of the rotational energy contained by the gain layer in models `m15_3D_rot_2deg` and `m15_3D_artrot_2deg` (Fig. 16). This quantity is at least one order of magnitude higher in model `m15_3D_artrot_2deg` during the linear growth phase of SASI spiral motions in the fast rotating case around 100 ms after bounce, underlining that the rotation velocities of the accreted material in model `m15_3D_rot_2deg` are too low to foster the creation of a spiral SASI mode. For such slow rotation with Rossby numbers $Ro \gg 1$, centrifugal forces play a negligible role and the critical luminosity to be reached for a successful shock runaway is hardly reduced compared to the nonrotating case (see also Sect. 4).

The stronger influence of rotation in model `m15_3D_artrot_2deg` cannot only be seen by the violent spiral SASI activity and a considerable overall reduction of the radiated neutrino luminosities and mean energies (Fig. 4), but also by a characteristic pole-to-equator variation of the neutrino emission. Rotation leads to a deformation of the proto-neutron

star and predominant accretion by the neutron star from the polar directions at later times, which leaves its imprint on the angle-dependent neutrino emission (see Fig. 17). In the depiction of the neutrino energy flux densities and mean energies versus polar angle, the fast rotating model exhibits a clear trough-like shape (see the detailed discussion of similar 2D results in section 3.6 of Marek & Janka 2009). Such an effect is not visible for model `m15_3D_rot_2deg`.

In analogy to the rotating 2D model discussed by Marek & Janka (2009), also in the 3D situation of model `m15_3D_artrot_2deg`, the polar accretion flows produce emission maxima for all neutrino species at angles between 20 and 40 degrees away from the pole, but these peaks are somewhat less sharp and lower than the emission maxima in the 2D case of Marek & Janka (2009). This difference might be a consequence of the unintended loss of angular momentum during the collapse phase in our present models, which reduces the rotational deformation of the newly formed neutron star compared to the previous publication.

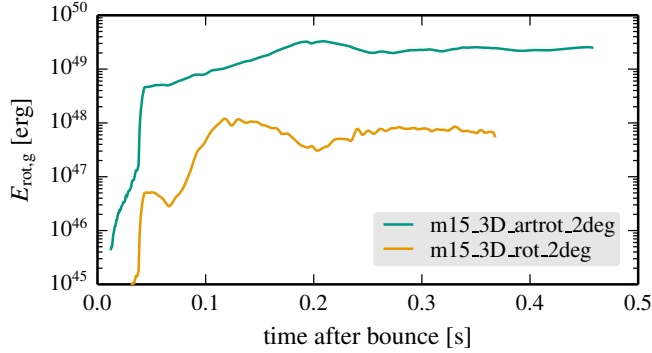


Figure 16. Time evolution of the rotational energy in the gain layer for the two best-resolved 3D models. The curves are smoothed by running averages of 5 ms.

In Fig. 8 (bottom panel), the diagnostic explosion energy versus time is plotted. It is given by

$$E_{\text{diag}} = \int_{V_g} e_{\text{tot}, > 0} \rho dV, \quad (16)$$

which is calculated as the integral of the total (i.e. kinetic plus internal plus gravitational) specific energy, defined as $e_{\text{tot}} = v^2/2 + \epsilon + \Phi$, over the gain layer, including all regions where this energy is positive. Following [Melson et al. \(2015b\)](#), we assume that all nucleons finally recombine to iron-group nuclei. At the time the simulation had to be stopped because of the extremely high computational demands, model `m15_3D_artrot_2deg` reaches a diagnostic energy of $\sim 9.3 \times 10^{49}$ erg, which is still rising steeply. Owing to the oblate explosion geometry (see Figs. 2 and 15), the ongoing accretion in the polar regions is not expected to cease soon. We therefore expect a considerable increase of the diagnostic energy even at later times after the onset of shock expansion as long as simultaneous accretion and shock expansion take place, an effect that was predicted by [Marek & Janka \(2009\)](#) and is seen in long-time 2D simulations ([Bruenn et al. 2016](#); [Nakamura et al. 2016](#)) as well as recent 3D simulations of nonrotating progenitors ([Müller 2015](#); [Müller et al. 2017](#)).

3.5. Resolution Dependence

Although we have briefly discussed resolution-dependent aspects of our results in the previous sections, we summarize the main points in the following. In 2D, the models with an angular resolution of 1.4 and 2 degrees evolve quite similarly (see Fig. 3, lower panel). While the better resolved simulations seem to exhibit a weak tendency to explode slightly earlier (Table 1), the observed differences between the two simulations for each rotation profile are in the ballpark of stochastic fluctuations (see [Summa et al. 2016](#)). In 3D, the setup chosen for the low-resolution runs with only 4 or 6 degrees in the angular domain (but the same radial res-

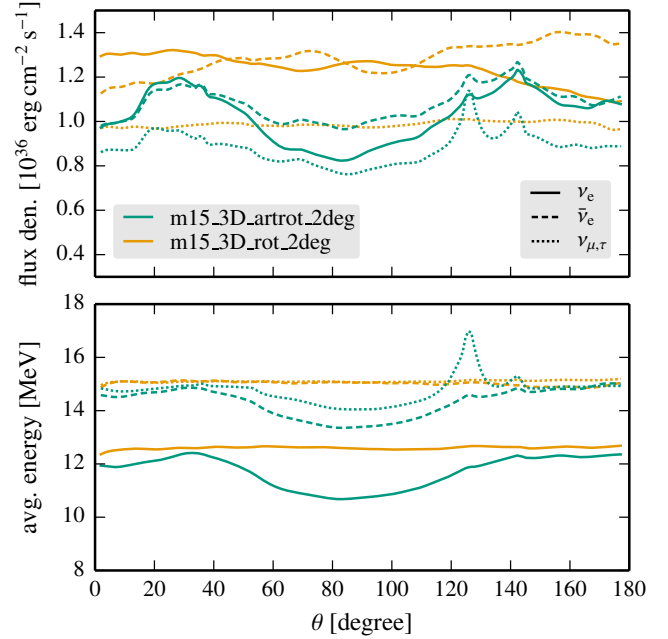


Figure 17. Neutrino energy flux densities and mean energies as functions of the polar angle at 365 ms after bounce. The lab-frame quantities are measured at a radius of 400 km and averaged over the azimuthal angle.

olution) was a compromise between the computational costs and our curiosity to investigate a larger set of models without real confidence in the numerical convergence of some of them. The coarseness of the grid for the less resolved models clearly has an impact on the temporal evolution. In the cases where a comparison is possible we find that the low-resolution models show a transient shock expansion up to 200 km after the initial shock retraction phase, in contrast to a better resolved model with an angular resolution of 2 degrees. The wider excursions of the average shock radius are a reaction to enhanced SASI activity during the corresponding time interval. We interpret this difference as a consequence of the suppressed growth of parasitic Rayleigh-Taylor and Kelvin-Helmholtz instabilities in models with lower angular resolution. In models with higher angular resolution these instabilities allow energy to cascade by turbulent fragmentation of vortex flows from the large SASI scales to smaller scales, thus damping the SASI amplitudes ([Guilet et al. 2010](#)). For this reason our low-resolution results have to be taken with caution and the major part of this paper focuses on the best-resolved 3D runs in our set with an angular resolution of 2 degrees.

4. THE CRITICAL NEUTRINO LUMINOSITY CONDITION REVISITED

Based on a toy model setup for steady-state accretion including neutrino heating behind the stalled accretion shock, [Burrows & Goshy \(1993\)](#) showed that for a given mass-accretion rate \dot{M} , there exists a critical neutrino

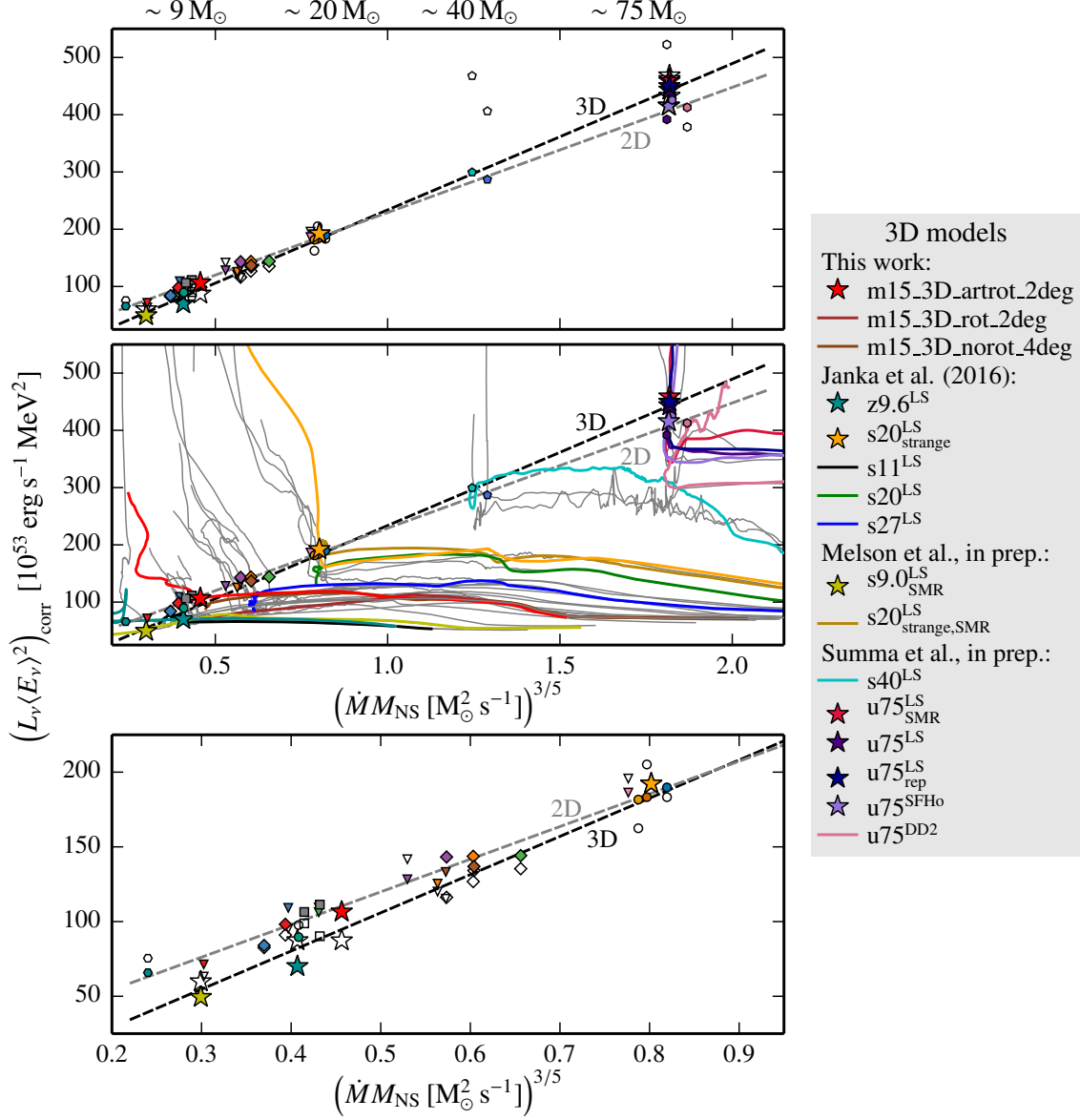


Figure 18. Critical luminosity relations for explosion or the onset of strong shock expansion, $(L_{\nu}\langle E_{\nu}^2 \rangle)_{\text{crit,corr}} \propto (\dot{M}M_{\text{NS}})^{3/5}$ of Eq. (30), for our considered sets of 2D (gray dashed line) and 3D simulations (black dashed line). The bottom panel provides a zoom to the progenitor-mass region of $\lesssim 20 M_{\odot}$. The lines are obtained by least-squares fits to the filled symbols for “corrected” values of the heating functional (Eq. 30) at the critical locations along the evolution tracks that are displayed by curves in the middle panel, considering 2D and 3D model sets separately. The best-fit lines of the available simulations show a modest dependence on dimension. The open symbols denote the uncorrected values of $(L_{\nu}\langle E_{\nu}^2 \rangle)_{\text{crit}}$. All symbols mark points on the evolution tracks when the time-scale ratio $\tau_{\text{adv}}/\tau_{\text{heat}}$ reaches a value of 1.2. Big colored asterisks and colored evolution tracks denote 3D models, whereas the small symbols and gray curves in the middle panel belong to 2D simulations. The list to the right of the panels provides an overview of all included 3D simulations (see text in Sect. 4.2). Cases with explosions (progenitors below $\sim 20 M_{\odot}$, see approximate mass scale above the top panel) or strong shock expansion (black-hole forming progenitors of $40\text{--}75 M_{\odot}$) have a line with an asterisk, the others just a line. The symbols and the color coding of the 2D models are adopted from figure 14 of Summa et al. (2016) and figure 3 of Janka et al. (2016) for previously published results (for details, see the list of models in Summa et al. (2016)). Symbols for black-hole forming 2D models possess the same colors as the corresponding 3D cases. We emphasize that the progenitor-mass scale on top of the figure is supposed to reflect only a rough, overall trend, in which lower-mass stars tend to be located towards the left while higher-mass stars tend to lie towards the right. However, local inversions with progenitor mass can occur because \dot{M} and M_{NS} correlate with the compactness of the stellar core (Nakamura et al. 2015), but the compactness is not a monotonic function of the progenitor mass (O’Connor & Ott 2011).

luminosity $L_{\nu, \text{crit}}(\dot{M})$ above which a stationary accretion flow onto the proto-neutron star is no longer possible. Janka (2012) demonstrated by analytic arguments that this critical luminosity condition is equivalent to the condition of $\tau_{\text{adv}}/\tau_{\text{heat}} \gtrsim 1$ for the ratio of advection and heating time scales (for hydrodynamical toy-model simulations in 1D leading to the same conclusion, see Fernández 2012).

4.1. Generalized Critical Heating Condition

In Müller & Janka (2015) this concept was generalized to a critical condition for the ‘heating functional’ $(L_{\nu}\langle E_{\nu}^2 \rangle)_{\text{crit}}$ in dependence on the mass-accretion rate \dot{M} , the proto-neutron star mass M_{NS} and the gain radius R_{g} . Because we compare results for different progenitors in the present work (in contrast to Müller & Janka 2015), we use the version of the critical condition introduced by Summa et al. (2016), equation 30, in which all gain-layer dependent properties are subsumed in a factor ξ_{g} :

$$(L_{\nu}\langle E_{\nu}^2 \rangle)_{\text{crit}} \propto (\dot{M}M_{\text{NS}})^{3/5} \xi_{\text{g}}. \quad (17)$$

With this definition, the correction factor ξ_{g} accounts for progenitor-dependent variations of the gain radius and turbulent effects that directly influence the critical neutrino luminosity.

Summa et al. (2016) and Janka et al. (2016) further generalized the critical condition to include the effects of rotation and to take care of case-dependent differences of the total energy at the gain radius. This was achieved by modifications of the correction factor ξ_{g} , whose exact functional form can be redefined to also account for the effects on the shock evolution associated with large-scale velocity perturbations in the convective Si and O burning shells prior to core collapse (Müller et al. 2016, 2017).

The main steps in deriving this critical luminosity can be summarized as follows. By the use of approximate scaling relations for the advection timescale τ_{adv} ,

$$\tau_{\text{adv}} \propto \frac{R_{\text{s}}^{3/2}}{\sqrt{\dot{M}_{\text{NS}}}}, \quad (18)$$

the heating timescale τ_{heat} ,

$$\tau_{\text{heat}} \propto \frac{|\bar{e}_{\text{tot,g}}| R_{\text{g}}^2}{L_{\nu}\langle E_{\nu}^2 \rangle}, \quad (19)$$

and the radius of the stalled shock in spherical symmetry,

$$R_{\text{s}} \propto \frac{(L_{\nu}\langle E_{\nu}^2 \rangle)^{4/9} R_{\text{g}}^{16/9}}{\dot{M}^{2/3} M_{\text{NS}}^{1/3}} \quad (20)$$

(see Janka 2012; Müller & Janka 2015), the timescale criterion $\tau_{\text{adv}}/\tau_{\text{heat}} \sim 1$ as conventional condition for runaway shock expansion (e.g. Thompson et al. 2005; Buras

et al. 2006b; Marek & Janka 2009; Fernández 2012) can directly be translated into a condition for the critical luminosity or heating functional:

$$(L_{\nu}\langle E_{\nu}^2 \rangle)_{\text{crit}} \propto (\dot{M}M_{\text{NS}})^{3/5} |\bar{e}_{\text{tot,g}}|^{3/5} R_{\text{g}}^{-2/5}. \quad (21)$$

Here, L_{ν} denotes the total luminosity of electron neutrinos and antineutrinos (because both of these neutrino species dominate the neutrino heating), $L_{\nu} = L_{\nu_e} + L_{\bar{\nu}_e}$, and $\langle E_{\nu}^2 \rangle$ is defined as the weighted average of the corresponding mean squared energies,

$$\langle E_{\nu}^2 \rangle = \frac{L_{\nu_e}\langle E_{\nu_e}^2 \rangle + L_{\bar{\nu}_e}\langle E_{\bar{\nu}_e}^2 \rangle}{L_{\nu_e} + L_{\bar{\nu}_e}}. \quad (22)$$

The mean squared energies stand for the squared energies of the neutrino-energy distributions, which can be expressed in terms of the energy moments of the neutrino-number distributions, $\langle E_{\nu_e}^2 \rangle := \langle \epsilon_{\nu_e}^3 \rangle / \langle \epsilon_{\nu_e} \rangle$ and $\langle E_{\bar{\nu}_e}^2 \rangle := \langle \epsilon_{\bar{\nu}_e}^3 \rangle / \langle \epsilon_{\bar{\nu}_e} \rangle$.

In addition to the dependence on the gain radius R_{g} and on the average mass-specific binding energy in the gain layer,

$$\bar{e}_{\text{tot,g}} = \frac{E_{\text{tot,g}}}{M_{\text{g}}}, \quad (23)$$

the time dependent factor ξ_{g} in Eq. (17) can absorb further corrections that are necessary to generalize the critical luminosity condition to the multidimensional case:

$$\xi_{\text{g}} \equiv |\bar{e}_{\text{tot,g}}|^{3/5} R_{\text{g}}^{-2/5} \xi_{\text{turb}}^{-3/5} \xi_{\text{rot}}^{6/5} \quad (24)$$

(Janka et al. 2016).

The consideration of nonradial (turbulent) postshock flows through an additional isotropic pressure contribution $P_{\text{turb}} \approx \langle v_{\text{aniso}}^2 \rangle \rho \approx 4/3 \langle \text{Ma}^2 \rangle P$ leads to the definition of ξ_{turb} (cf. Müller & Janka 2015),

$$\xi_{\text{turb}} \equiv 1 + \frac{4}{3} \langle \text{Ma}^2 \rangle, \quad (25)$$

where we follow Janka et al. (2016) by using the definition

$$\begin{aligned} \langle \text{Ma}^2 \rangle &= \frac{\langle v_{\text{aniso}}^2 \rangle}{\langle c_{\text{s,g}}^2 \rangle} = \frac{1}{\langle c_{\text{s,g}}^2 \rangle} \sum_{i=r,\theta,\phi} \langle (v_i - \bar{v}_i)^2 \rangle \\ &= \frac{2E_{\text{kin,g}}^{\text{aniso}}/M_{\text{g}}}{\langle c_{\text{s,g}}^2 \rangle}. \end{aligned} \quad (26)$$

$\bar{v}_{r,\theta,\phi}$ are angular averages over spherical shells, i.e. ordered radial flows due to accretion or the expansion of the gain layer and coherent angular motions caused by stellar rotation or spiral SASI modes are subtracted. The sound speed $c_{\text{s,g}}$ is directly extracted from the numerical simulations as a mass-weighted average over the gain layer:

$$\langle c_{\text{s,g}}^2 \rangle = \frac{1}{M_{\text{g}}} \int_{V_{\text{g}}} c_{\text{s}}^2 \rho \, dV. \quad (27)$$

Note that in contrast to Müller & Janka (2015) and Müller (2016); Müller et al. (2017) we prefer to evaluate $\langle c_{s,g}^2 \rangle$ as numerical average over the gain layer instead of estimating a postshock value from the shock-jump conditions. The volume-integrated approach makes the analysis numerically more robust, but might not be fully compatible with the fact that local properties at the gain radius or behind the shock could more directly determine the dynamical behavior.

The effects of rotation are included by an additional correction factor

$$\xi_{\text{rot}} \equiv \sqrt{1 - \frac{j_0^2}{2GM_{\text{NS}}R_s}} \leq 1, \quad (28)$$

where j_0 is defined as the average specific momentum on spherical shells, which is essentially conserved during the infall of the matter in the pre-collapse region. The factor ξ_{rot} accounts for the reduction of the infall velocity ahead of the stalled shock due to centrifugal effects, which leads to an increase of the accretion time scale in the postshock layer (Eq. 18) as well as to an increase of the shock-stagnation radius (Eq. 20). For a detailed discussion, see Janka et al. (2016).

As also detailed in Janka et al. (2016), rotation therefore decreases the critical luminosity necessary for a runaway shock expansion or a successful explosion. Besides the effects of rotation taken into account by the correction factor ξ_{rot} mentioned above, rotational energy in the gain layer also shifts the (negative) total specific energy $\bar{e}_{\text{tot,g}}$ closer to zero and leads to an additional reduction of the critical luminosity (see Eqs. 17 and 24).

4.2. Critical Luminosity Relation for a Large Set of Models

With a growing set of multidimensional simulations becoming available, we can test the validity of the critical condition (Eq. 17 with Eq. 24) for an increasingly wider range of progenitor conditions. While Summa et al. (2016) already used a larger sample of 2D models, we include here our 2D and 3D cases with rotation. Moreover, we also take into account 3D results of non-rotating 9 and 20 M_{\odot} stars as well as calculations for black-hole forming 40 and 75 M_{\odot} progenitors (Woosley et al. 2002; Woosley & Heger 2007), all of which will be published in detail in forthcoming papers (Melson et al., in preparation, and Summa et al., in preparation, respectively). In the model names, the superscripts denote the employed high-density EoSs. LS indicates the EoS of Lattimer & Swesty (1991) with a nuclear incompressibility of 220 MeV, SFHo the EoS introduced by Hempel et al. (2012) and Steiner et al. (2013), and DD2 the EoS provided by Typel et al. (2010) and Fischer et al. (2014). The subscript ‘‘SMR’’ refers to the application of a static angular mesh refinement tech-

nique for the computational grid (Melson 2016), and the subscript ‘‘strange’’ denotes the use of a reduced neutral-current neutrino-nucleon scattering opacity motivated by possible strangeness contributions to the nucleon spin, which affect the axial-vector weak coupling (Melson et al. 2015a). In the case of model u75_{rep}^{LS}, the subscript just indicates a repetition of model u75^{LS} with a parallelization over the energy bins, which was newly implemented in our neutrino-transport code.

Including these still unpublished results allows us to considerably widen the range of values considered in the $(L_{\nu}\langle E_{\nu}^2 \rangle) - (\dot{M}M_{\text{NS}})^{3/5}$ -plane. The black-hole forming 2D and 3D models partially exhibit a shock-expansion phase in which $\tau_{\text{adv}}/\tau_{\text{heat}}$ can exceed unity. This is caused by violent SASI spiral and sloshing activity shortly before the neutron star becomes gravitationally unstable and its collapse sets in. Despite therefore fulfilling the critical condition for shock expansion, we do not expect these models to produce supernova explosions.

In the critical condition of Eq. (17), the critical value of the heating functional varies not only as a function of $(\dot{M}M_{\text{NS}})$, but also with the diverse effects accounted for by the factors assembled in ξ_g (Eq. 24), which differ between progenitors and depend on the strength of nonradial instabilities, rotation, and on dimensionality. Following Summa et al. (2016) and Janka et al. (2016), we therefore construct a universal relation by normalizing $(L_{\nu}\langle E_{\nu}^2 \rangle)$ by the factor ξ_g/ξ_g^* , where

$$\xi_g^* \equiv |\bar{e}_{\text{tot,g}}|^{3/5} R_g^{-2/5} \xi_{\text{turb}}^{-3/5} \xi_{\text{rot}}^{6/5} \Big|_{\tau_{\text{adv}}/\tau_{\text{heat}}=1.2}^{\text{s20}_{\text{strange}}^{\text{LS}}} \quad (29)$$

is a constant introduced in order to define a reference case by the critical point of a (arbitrarily) chosen reference model. Our universal critical relation therefore becomes

$$(L_{\nu}\langle E_{\nu}^2 \rangle)_{\text{crit,corr}} \equiv \frac{1}{\xi_g/\xi_g^*} (L_{\nu}\langle E_{\nu}^2 \rangle)_{\text{crit}} \propto (\dot{M}M_{\text{NS}})^{3/5}. \quad (30)$$

for the ‘‘corrected’’ heating functional $(L_{\nu}\langle E_{\nu}^2 \rangle)_{\text{crit,corr}}$.

Note that, in contrast to Summa et al. (2016) and Janka et al. (2016), we evaluate ξ_g^* here at the time when $\tau_{\text{adv}}/\tau_{\text{heat}} = 1.2$ (instead of unity). Considering our larger set of simulations it turns out that some of them exceed a time-scale ratio of $\tau_{\text{adv}}/\tau_{\text{heat}} = 1$ transiently although they do not reach explosion conditions immediately. With the empirically chosen value of 1.2, we can well capture the critical behavior of all models of our set by the proportionality relation of Eq. (30) (see Fig. 18). For the reference case, we picked the 3D model s20_{strange}^{LS} (Melson et al. 2015a). Besides the rotating models of the present work (m15_3D_artrot_2deg as only exploding 3D case in red, m15_3D_rot_2deg in brown, m15_3D_norot_4deg in saddle brown; the exploding 2D models m15_2D_rot_2deg and m15_2D_norot_2deg are

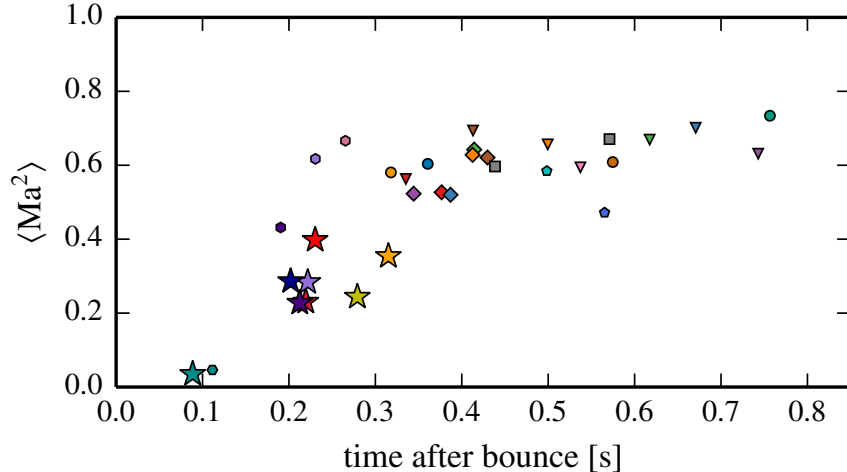


Figure 19. Average squared turbulent Mach number in the gain layer at the time when the ratio $\tau_{\text{adv}}/\tau_{\text{heat}}$ reaches a value of 1.2 for all models displayed in Fig. 18. For the symbols and color coding, see caption of Fig. 18.

identified by gray squares at their critical conditions), the list of 3D simulations in Fig. 18 denotes models $z9.6^{\text{LS}}$ and $s20_{\text{strange}}^{\text{LS}}$ as exploding cases of Melson et al. (2015b,a), models $s11^{\text{LS}}$, $s20^{\text{LS}}$, and $s27^{\text{LS}}$ as nonexploding simulations discussed by Tamborra et al. (2014a,b) and Hanke et al. (2013), models $s9.0_{\text{SMR}}^{\text{LS}}$ and $s20_{\text{strange,SMR}}^{\text{LS}}$ from Melson (2016) and the black-hole forming cases $s40^{\text{LS}}$, $u75_{\text{SMR}}^{\text{LS}}$, $u75^{\text{LS}}$, $u75_{\text{rep}}^{\text{LS}}$, $u75^{\text{SFHo}}$, and $u75^{\text{DD2}}$ from Summa et al. (in preparation).

Fig. 18 shows the results of our analysis. In the upper panel, the uncorrected (open symbols) as well as the corrected values (filled symbols) for the heating functional at the onset of shock runaway are given for our set of exploding 3D (big asterisks) and 2D models (all other symbols). The correction procedure shows the desired effect: The scatter of the points is significantly reduced (see especially the large corrections for the points in the right half of the plot and the bottom panel for a zoom to the lower left region of the top panel). 2D as well as 3D models can be fitted by a straight line which separates models with explosion or strong shock expansion from those with shock retraction.

When evolving along the evolution track (curves for $(L_{\nu}\langle E_{\nu}^2 \rangle)_{\text{corr}}$ versus $(\dot{M}M_{\text{NS}})^{3/5}$ in the middle panel of Fig. 18; the evolution runs from the right to the left), the models hit the critical condition for shock runaway at the moment they reach the critical line. The evolution tracks then (usually) bend sharply upwards because the correction factor $\xi_{\text{g}}/\xi_{\text{g}}^*$ in the denominator on the rhs of Eq. (30) becomes very small due to ξ_{turb} strongly increasing and $|\bar{e}_{\text{tot,g}}|$ tending towards zero as more and more matter in the gain layer becomes marginally bound (for a detailed description, see Summa et al. 2016).

Our large sample of explosion models shows that the slopes of the critical lines for 2D (gray dashed line) and 3D (black dashed line) models are slightly differ-

ent. This is not surprising since Eq. (30) only provides a proportionality relation where the proportionality constant is not fixed. Therefore differences in the explosion behavior of 2D and 3D simulations can manifest themselves in different slopes of the best-fit straight lines. The separate fitting of 2D and 3D models also reduces the discrepancies between the universal critical curve and the 3D data points that are visible at low $(L_{\nu}\langle E_{\nu}^2 \rangle)_{\text{corr}}$ and $(\dot{M}M_{\text{NS}})^{3/5}$ values in figure 3 of Janka et al. (2016), which was only based on a reduced model set.

The difference of the critical curves for 2D and 3D models may be connected to a difference in the turbulent Mach number values at the beginning of explosion (see Fig. 19): In 2D, these values are (on average) a factor of about two higher than in 3D. This implies smaller values of ξ_{turb} (Eq. 25) and therefore bigger values of ξ_{g} (Eq. 24) for 3D models at their critical points, leading to smaller values of the corrected heating functional $(L_{\nu}\langle E_{\nu}^2 \rangle)_{\text{crit,corr}}$ (Eq. 30). In the black-hole forming massive stars this trend is reversed, because in these cases extremely strong SASI activity and the associated kinetic energy pushes $|\bar{e}_{\text{tot,g}}|$ closer to zero. Our observation that 3D models can reach critical conditions for shock expansion in spite of smaller turbulent Mach numbers is compatible with similar findings by Müller et al. (2016) and Müller et al. (2017), who reported a smaller scaling factor between $E_{\text{kin,g}}^{\text{aniso}}/M_{\text{g}}$ and $(\dot{Q}_{\text{heat}}/M_{\text{g}})^{2/3}$ in 3D compared to 2D. These facts could imply that in 3D other effects connected to turbulence might be more relevant than turbulent pressure, for example turbulent dissipation (Mabanta & Murphy 2017) or more efficient convective heat transport (cf. Murphy et al. 2013). It is interesting that in the context of this discussion the “two-dimensionalization” of turbulent motions and of the corresponding power spectrum of the kinetic energy

(Eq. 6, Fig. 12) that is associated with enhanced rotation in the case of model `m15u6_3D_artrot_2deg` seems to manifest itself: In terms of turbulent Mach number, this model (red asterisk in Fig. 19) is closest to the cloud of points of the 2D models, and also in Fig. 18 the fast rotating 3D model is very close to the critical line for the 2D cases.

In view of the simple correction factors we applied to account for model-to-model variations with respect to nonradial mass motions, rotation, and further gain-layer related quantities, the resulting critical lines capture the runaway behavior of all models remarkably well and confirm the existence of a (slightly dimension-dependent) universal criterion for the development of critical conditions in our large set of 2D and 3D simulations.

5. CONCLUSIONS

Making use of three-flavor, energy dependent, ray-by-ray-plus neutrino transport including the full set of state-of-the-art neutrino reactions and microphysics, we have studied the influence of rotation on the explosion dynamics of a $15 M_{\odot}$ progenitor (Heger et al. 2005) by hydrodynamic simulations of the neutrino-heating mechanism in 2D and 3D. Besides using the rotation profile provided by the progenitor model, in which magnetic field effects on the angular momentum evolution had been taken into account up to the onset of core collapse, we also performed simulations without rotation and with a roughly 300 times higher angular momentum ($\sim 2 \times 10^{16} \text{ cm}^2 \text{ s}^{-1}$, corresponding to a spin period of ~ 20 s, instead of $\sim 6 \times 10^{13} \text{ cm}^2 \text{ s}^{-1}$ and ~ 6000 s) at the explosion-relevant Si/Si-O composition interface prior to collapse.

Our results suggest that sufficiently rapid rotation (as in our model with artificially increased spin rate) favors the growth of strong SASI spiral activity in the equatorial plane and that the appearance of such SASI modes has an important influence on the explosion. The dependence of success or failure on the stellar spin rate is largely different between 2D (where nonaxisymmetric instabilities are absent) and 3D, and it is also different from results of simplified toy-model studies (using neutrino light bulbs) where feedback effects of rotation on the neutrino emission are not taken into account.

“Moderate” rotation as present in the original progenitor model has no significant influence on the development of the supernova blast. In 2D, we obtained explosions for the nonrotating as well as moderately rotating cases (for the latter case roughly 150 ms earlier, but this is basically within the range of stochastic fluctuations between different 2D simulations with slightly varied conditions, see Summa et al. 2016). The 2D run with artificially increased rotation, however, did not explode until nearly 500 ms after core bounce, because cen-

trifugal effects on the postshock accretion flow and the centrifugal deformation of the neutrinospheric layer reduce the neutrino luminosities and mean energies and thus the neutrino heating in the gain layer.

In 3D, in contrast, neither the nonrotating nor the moderately rotating models showed any tendency to explode until ~ 400 ms after bounce, in line with the 2D-3D differences previously obtained by the Garching group for 11.2 , 20 , and $27 M_{\odot}$ progenitors simulated with the same microphysics and numerical setup (except for the use of a Yin-Yang grid and a smaller 1D core of only 1.6 km radius in the present 3D runs). Different from the 2D behavior, however, the 3D simulation with the artificially increased rotation rate developed an explosion on a relatively short time scale of roughly 200 ms after bounce, when the infalling Si/Si-O interface reaches the shock wave. This success is facilitated by the strong spiral SASI motions of the postshock layer, which store gravitational binding energy of the accretion flow in kinetic energy of rotation. The spiral SASI pushes the shock outwards and thus increases the volume and mass of the gain layer. This allows for a higher neutrino heating rate and heating efficiency despite the rotationally reduced neutrino luminosities and mean energies. Moreover, it also stores gravitational binding energy of the accretion flow in kinetic energy of rotation and thus raises the total specific energy of the matter in the gain layer, which drives the conditions closer to the threshold for an explosion. These findings are consistent with conclusions drawn by Fernández (2015).

The spiral SASI in our most rapidly spinning model supports shock expansion most strongly in the equatorial plane, i.e., it triggers an oblate deformation, which is in distinct contrast to simulations of explosions of fast rotating stars in 2D, where a prolate shape of the outgoing blast wave is obtained (see Fig. 2). This fundamental difference was already pointed out by Nakamura et al. (2014). Interestingly, in our 3D model with rapid rotation and a Rossby number of $\text{Ro} \lesssim 1$, we observe a “two-dimensionalization” of the power spectrum of the turbulent kinetic energy, which resembles the ~ -3 power-law decline at intermediate wavelengths that is characteristic of the 2D case (Fig. 12). This reflects the fact that the presence of centrifugal and coriolis forces constrains the degrees of freedom for the turbulent fluid motions, and, similar to the 2D case, considerably more kinetic energy is stored on the largest possible scales encompassed by the SASI spiral structures.

Although at later times in our fast-spinning model a corotation radius between the SASI-deformed shock and the proto-neutron star surface can be identified, interior to which the matter orbits with shorter periods than the characteristic spiral-SASI pattern of the shock, our model does not develop a tightly-wound, one-armed spi-

ral pattern as observed in considerably faster spinning environments by Takiwaki et al. (2016) and Kazeroni et al. (2017). The small number of 3D simulations that we could perform with our detailed neutrino physics, as well as limitations of the numerical resolution that is affordable in these simulations (which might affect the growth of instabilities to an extent we currently cannot quantify) do not permit us to add substantial insights to a better and more systematic understanding of the subtle interplay between rotation, the spiral SASI mode, and the corotational instability as suggested by the recent works of Takiwaki et al. (2016), Blondin et al. (2017) and Kazeroni et al. (2017). Further studies of the different regimes of these instabilities are certainly desirable.

The high rotation rate adopted for our exploding 3D model leads to a final neutron star spin period of less than ~ 5 ms if angular momentum conservation is assumed. This is considerably faster than the initial spin periods estimated for radio pulsars associated with supernova remnants, which are in the ballpark of several tens to several hundreds of milliseconds (Popov & Turolla 2012). Since efficient spin-down mechanisms of newborn neutron stars are not known (see Heger et al. 2005; Ott et al. 2006; Kazeroni et al. 2017), the large angular momentum artificially imposed on the progenitor core of our fast rotating model does not seem to be representative of the birth sites for the majority of observed neutron stars.

With a growing set of fully self-consistent 3D core-collapse simulations at hand, including previously published Garching models, the discussed models with rotation of the present work, and more still unpublished results of nonrotating low-mass as well as black-hole forming progenitors (Melson et al., in preparation; Summa et al., in preparation, respectively), we were able to extend our analysis of a critical luminosity condition for 2D models in Summa et al. (2016) to the full set of 2D and 3D calculations. We confirmed our previous finding that a simple power-law relation (critical curve) between the “corrected” critical heating functional, $(L_\nu \langle E_\nu^2 \rangle)_{\text{crit,corr}}$, and the product of preshock mass-accretion rate and neutron star mass, $(\dot{M} M_{\text{NS}})$, as expressed by Eq. (30), separates the domain where the supernova shock evolves as stalled accretion shock from the domain of runaway shock expansion. This critical curve, which forms a straight line in the $(L_\nu \langle E_\nu^2 \rangle)_{\text{corr}} - (\dot{M} M_{\text{NS}})^{3/5}$ -plane, captures, with amazingly little scatter, the critical points for the transition between both regimes of shock behavior for progenitors from the $9 M_\odot$ range up to $75 M_\odot$

(Fig. 18)³. The correction factor applied to the heating functional accounts for effects of turbulent pressure, rotation, and progenitor-dependent variations of the gain radius and total specific energy of the material in the gain layer.

We diagnose a slight difference between the critical curves of 2D and 3D models: the critical condition for 3D models is somewhat steeper in the $(L_\nu \langle E_\nu^2 \rangle)_{\text{corr}} - (\dot{M} M_{\text{NS}})^{3/5}$ -space. On the one hand this is connected to the fact that the turbulent Mach numbers in the gain layer at the time of shock runaway are typically a factor of roughly two lower for 3D models (Fig. 19). This decreases their correction factors in Eq. (30) and shifts the 3D critical line below the 2D critical line for lower-mass stars (corresponding to the low side of the $(\dot{M} M_{\text{NS}})^{3/5}$ scale). On the other hand, in higher-mass (black-hole forming) progenitors powerful sloshing and spiral SASI mass motions drive the shock expansion and raise the (negative) total specific energy in the gain layer closer to zero by contributing significant amounts of kinetic energy. This increases their correction factors and lifts the critical line for 3D models above the one of the 2D counterparts on the high side of the $(\dot{M} M_{\text{NS}})^{3/5}$ space. The difference in the turbulent Mach numbers between 2D and 3D at the onset of shock runaway indicates that turbulent effects and nonradial mass motions manifest themselves in their effects on the supernova shock dynamics in different ways in 2D and 3D simulations, potentially pointing to a higher relevance of turbulent pressure effects in 2D, whereas in 3D turbulent heat transport and spiral SASI activity may play a more important role. Consistent with the “two-dimensionalization” of the turbulent power spectrum, rapid rotation with its constraints on the (turbulent) mass motions in the gain layer moves our corresponding 3D model closer to the critical behavior of the subset of 2D cases.

We are grateful to T. Foglizzo and R. Kazeroni for helpful discussions and thank A. Döring for the visualizations of Figs. 14 and 15. The project was supported by the Deutsche Forschungsgemeinschaft through the Excellence Cluster Universe (EXC 153; <http://www.universe-cluster.de/>) and by the European Research Council through grant ERC-AdG No. 341157-COCO2CASA. We acknowledge computing time through the European PRACE initiative on SuperMUC (GCS@LRZ, Germany) and MareNostrum (BSC-CNS, Spain) and through the Gauss Centre for Supercom-

³ Investigated progenitors with 40 and $75 M_\odot$ do not develop explosions, but can exhibit large-amplitude shock expansion driven by violent SASI activity prior to black-hole formation. Details will be reported in a forthcoming publication by Summa et al. (in preparation).

puting (GCS) on SuperMUC at the Leibniz Supercomputing Centre (LRZ). Postprocessing was done on Hydra of the Max Planck Computing and Data Facility (MPCDF).

Software: PROMETHEUS-VERTEX (Fryxell et al. 1989; Rampp & Janka 2002; Buras et al. 2006b), NumPy and Scipy (Oliphant 2007), IPython (Perez & Granger 2007), Matplotlib (Hunter 2007).

REFERENCES

- Akiyama, S., Wheeler, J. C., Meier, D. L., & Lichtenstadt, I. 2003, *ApJ*, 584, 954
- Blondin, J. M., Gipson, E., Harris, S., & Mezzacappa, A. 2017, *ApJ*, 835, 170
- Blondin, J. M., & Mezzacappa, A. 2007, *Nature*, 445, 58
- Bollig, R., Janka, H.-T., Lohs, A., et al. 2017, *ArXiv e-prints*, arXiv:1706.04630
- Bruenn, S. W., Lentz, E. J., Hix, W. R., et al. 2016, *ApJ*, 818, 123
- Buras, R., Janka, H.-T., Rampp, M., & Kifonidis, K. 2006a, *A&A*, 457, 281
- Buras, R., Rampp, M., Janka, H.-T., & Kifonidis, K. 2006b, *A&A*, 447, 1049
- Burrows, A., Dolence, J. C., & Murphy, J. W. 2012, *ApJ*, 759, 5
- Burrows, A., & Goshy, J. 1993, *ApJL*, 416, L75
- Cantiello, M., Mankovich, C., Bildsten, L., Christensen-Dalsgaard, J., & Paxton, B. 2014, *ApJ*, 788, 93
- Couch, S. M., Chatzopoulos, E., Arnett, W. D., & Timmes, F. X. 2015, *ApJL*, 808, L21
- Couch, S. M., & Ott, C. D. 2013, *ApJL*, 778, L7
- Dessart, L., Burrows, A., Livne, E., & Ott, C. D. 2006, *ApJ*, 645, 534
- . 2007, *ApJ*, 669, 585
- Fernández, R. 2012, *ApJ*, 749, 142
- . 2015, *MNRAS*, 452, 2071
- Fischer, T., Hempel, M., Sagert, I., Suwa, Y., & Schaffner-Bielich, J. 2014, *European Physical Journal A*, 50, 46
- Fryxell, B., Müller, E., & Arnett, W. 1989, *Hydrodynamics and Nuclear Burning* (Garching: Max-Planck-Institut für Astrophysik)
- Godefert, F. S., & Moisy, F. 2015, *Applied Mechanics Reviews*, 67, 030802
- Guilet, J., Sato, J., & Foglizzo, T. 2010, *ApJ*, 713, 1350
- Hanke, F., Marek, A., Müller, B., & Janka, H.-T. 2012, *ApJ*, 755, 138
- Hanke, F., Müller, B., Wongwathanarat, A., Marek, A., & Janka, H.-T. 2013, *ApJ*, 770, 66
- Heger, A., Woosley, S. E., & Spruit, H. C. 2005, *ApJ*, 626, 350
- Hempel, M., Fischer, T., Schaffner-Bielich, J., & Liebendörfer, M. 2012, *ApJ*, 748, 70
- Hunter, J. D. 2007, *Computing in Science & Engineering*, 9, 90
- Iwakami, W., Kotake, K., Ohnishi, N., Yamada, S., & Sawada, K. 2009, *ApJ*, 700, 232
- Iwakami, W., Nagakura, H., & Yamada, S. 2014, *ApJ*, 793, 5
- Janka, H.-T. 2012, *Annual Review of Nuclear and Particle Science*, 62, 407
- Janka, H.-T., Melson, T., & Summa, A. 2016, *Annual Review of Nuclear and Particle Science*, 66, 341
- Kageyama, A., & Sato, T. 2004, *Geochem. Geophys. Geosys.*, 5
- Kazeroni, R., Guilet, J., & Foglizzo, T. 2017, *ArXiv e-prints*, arXiv:1701.07029
- Kotake, K., Sato, K., & Takahashi, K. 2006, *Reports on Progress in Physics*, 69, 971
- Kraichnan, R. H. 1967, *Physics of Fluids*, 10, 1417
- Kuroda, T., Takiwaki, T., & Kotake, K. 2014, *PhRvD*, 89, 044011
- Landau, L. D., & Lifshitz, E. M. 1959, *Fluid mechanics* (Course of theoretical physics, Oxford: Pergamon Press)
- Lattimer, J. M., & Prakash, M. 2001, *ApJ*, 550, 426
- Lattimer, J. M., & Swesty, F. D. 1991, *Nuclear Physics A*, 535, 331
- Lentz, E. J., Bruenn, S. W., Hix, W. R., et al. 2015, *ApJL*, 807, L31
- Mabanta, Q., & Murphy, J. W. 2017, *ArXiv e-prints*, arXiv:1706.00072
- Marek, A., Dimmelmeier, H., Janka, H.-T., Müller, E., & Buras, R. 2006, *A&A*, 445, 273
- Marek, A., & Janka, H.-T. 2009, *ApJ*, 694, 664
- Melson, T., Janka, H.-T., Bollig, R., et al. 2015a, *ApJL*, 808, L42
- Melson, T., Janka, H.-T., & Marek, A. 2015b, *ApJL*, 801, L24
- Melson, T. F. 2016, *Dissertation*, Technische Universität München, München
- Mösta, P., Ott, C. D., Radice, D., et al. 2015, *Nature*, 528, 376
- Mösta, P., Richers, S., Ott, C. D., et al. 2014, *ApJL*, 785, L29
- Müller, B. 2015, *MNRAS*, 453, 287
- . 2016, *PASA*, 33, e048
- Müller, B., & Janka, H.-T. 2015, *MNRAS*, 448, 2141
- Müller, B., Janka, H.-T., & Marek, A. 2012, *ApJ*, 756, 84
- Müller, B., Melson, T., Heger, A., & Janka, H.-T. 2017, *ArXiv e-prints*, arXiv:1705.00620
- Müller, B., Viallet, M., Heger, A., & Janka, H.-T. 2016, *ApJ*, 833, 124
- Müller, E., Rampp, M., Buras, R., Janka, H.-T., & Shoemaker, D. H. 2004, *ApJ*, 603, 221
- Murphy, J. W., Dolence, J. C., & Burrows, A. 2013, *ApJ*, 771, 52
- Nakamura, K., Horiuchi, S., Tanaka, M., et al. 2016, *MNRAS*, 461, 3296
- Nakamura, K., Kuroda, T., Takiwaki, T., & Kotake, K. 2014, *ApJ*, 793, 45
- Nakamura, K., Takiwaki, T., Kuroda, T., & Kotake, K. 2015, *PASJ*, psv073, arXiv:1406.2415
- Obergaulinger, M., & Aloy, M. Á. 2017, *MNRAS*, 469, L43
- O’Connor, E., & Ott, C. D. 2011, *ApJ*, 730, 70
- Oliphant, T. E. 2007, *Computing in Science and Engg.*, 9, 10
- Ott, C. D., Burrows, A., Thompson, T. A., Livne, E., & Walder, R. 2006, *ApJS*, 164, 130
- Ott, C. D., Abdikamalov, E., Mösta, P., et al. 2013, *ApJ*, 768, 115
- Perez, F., & Granger, B. E. 2007, *Computing in Science and Engg.*, 9, 21
- Popov, S. B., & Turolla, R. 2012, *Ap&SS*, 341, 457
- Rampp, M., & Janka, H.-T. 2002, *A&A*, 396, 361
- Roberts, L. F., Ott, C. D., Haas, R., et al. 2016, *ApJ*, 831, 98
- Rubio, A. M., Julien, K., Knobloch, E., & Weiss, J. B. 2014, *Physical Review Letters*, 112, 144501
- Smith, L. M., & Waleffe, F. 1999, *Physics of Fluids*, 11, 1608
- Steiner, A. W., Hempel, M., & Fischer, T. 2013, *ApJ*, 774, 17
- Summa, A., Hanke, F., Janka, H.-T., et al. 2016, *ApJ*, 825, 6
- Takiwaki, T., Kotake, K., & Suwa, Y. 2012, *ApJ*, 749, 98
- . 2014, *ApJ*, 786, 83
- . 2016, *MNRAS*, 461, L112
- Tamborra, I., Hanke, F., Janka, H.-T., et al. 2014a, *ApJ*, 792, 96
- Tamborra, I., Raffelt, G., Hanke, F., Janka, H.-T., & Müller, B. 2014b, *PhRvD*, 90, 045032
- Thompson, T. A., Quataert, E., & Burrows, A. 2005, *ApJ*, 620, 861

Typel, S., Röpke, G., Klähn, T., Blaschke, D., & Wolter, H. H. 2010, *PhRvC*, 81, 015803
Winteler, C., Käppeli, R., Perego, A., et al. 2012, *ApJL*, 750, L22
Wongwathanarat, A., Hammer, N. J., & Müller, E. 2010, *A&A*, 514, A48
Woosley, S. E., & Heger, A. 2007, *PhR*, 442, 269

Woosley, S. E., Heger, A., & Weaver, T. A. 2002, *Reviews of Modern Physics*, 74, 1015
Zeman, O. 1994, *Physics of Fluids*, 6, 3221